

TOPOLOGICAL DECODING OF GRID CELL ACTIVITY VIA PATH LIFTING TO COVERING SPACES

YUXING JARED YAO^{1,3}, IRIS H.R. YOON^{1,2*}

¹Department of Mathematics and Computer Science, Wesleyan University

²Department of Mathematics and Statistics, Swarthmore College

³Program in Neuroscience and Behavior, Wesleyan University

ABSTRACT. High-dimensional neural activity often reside in a low-dimensional subspace, referred to as neural manifolds. Grid cells in the medial entorhinal cortex provide a periodic spatial code that are organized near a toroidal manifold, independent of the spatial environment. Due to the periodic nature of its code, it is unclear how the brain utilizes the toroidal manifold to understand its state in a spatial environment. We introduce a novel framework that decodes spatial information from grid cell activity using topology. Our approach uses topological data analysis to extract toroidal coordinates from grid cell population activity and employs path-lifting to reconstruct trajectories in physical space. The reconstructed paths differ from the original by an affine transformation. We validated the method on both continuous attractor network simulations and experimental recordings of grid cells, demonstrating that local trajectories can be reliably reconstructed from a single grid cell module without external position information or training data. These results suggest that co-modular grid cells contain sufficient information for path integration and suggest a potential computational mechanism for spatial navigation.

1. INTRODUCTION

Activity of a population of neurons often reside in a low-dimensional subspace called a neural manifold [7, 15, 17, 18, 25, 28, 37, 40] whose structure reflects the information encoded by the neurons. For example, the activity of head direction cells [35] are organized near a circle [7, 28]. Grid cells in the medial entorhinal cortex (MEC) exhibit a periodic hexagonal firing pattern that tiles the environment at regular intervals [17] and are organized into modules whose cells share scale and orientation but differ by fixed spatial phase offsets [17, 22]. The periodicity of a single-module of grid cell activity implies that the population activity is topologically organized around a torus ¹ [4, 14]. Such organization has been captured by continuous attractor network (CAN) models of grid cells and have been observed in large-scale recordings [15].

Because multiple locations in a spatial environment elicit a similar response among co-modular grid cells, spatial locations are not uniquely encoded in the toroidal neural manifold of grid cells. This insight raise a central question: how much spatial information can be decoded from the activity of a single module of grid cells? Prior efforts to decode position from neural activity often relied on place cell dynamics [1, 8, 11, 31] or on combining phase differences across multiple grid modules [21, 32]. Other methods perform cumulative vector integration [5] or train deep models to map activity to position [13, 19, 23, 34, 39]. Theoretical analysis indicates that single grid module may carry sufficient information to update its internal representation of position [5, 12, 20, 33], known as path-integration, though explicit computational demonstrations have been limited, constrained to multiple trials of one-dimensional settings [38] or relying on access to firing rate maps and training of deep neural networks [26].

In this study, we present a novel method for decoding movement trajectories from the activity of a single module of grid cells. The method integrates tools from topological data analysis and path lifting in topology: Persistent cohomology reveals the toroidal structure of grid cell activity,

¹A torus is a space that represents the outside surface of a donut. Here, we represent a torus by identifying the left and right edges and by identifying the top and bottom edges of a parallelogram

circular and toroidal coordinates parametrize grid cell activity on this torus, and path lifting reconstructs the movement path in Euclidean space. To the authors' knowledge, this is the first work integrating path lifting in topology into computational and applied settings. The approach differs from existing decoding work in that it only uses data from a single module of grid cells and that it doesn't involve any training process. We validate the algorithm in both CAN-simulated and experimental datasets by showing that the reconstructed movement paths differ from the original by an affine transformation. The work highlights the sufficiency of co-modular grid cells for path integration.

2. RESULTS

2.1. An internal representation of space can be constructed from grid cell activity. We present a novel algorithm that reconstructs movement trajectories from grid cell activity (Fig. 1). The method proceeds in two stages. First, using persistent cohomology and toroidal coordinates, we assign toroidal coordinates to each population vector. This constructs a path on the grid cell torus as the subject moves (Fig. 1A-D). Second, we “lift” this path on the torus to the plane, thereby reconstructing the subject's movement in physical space (Fig. 1E).

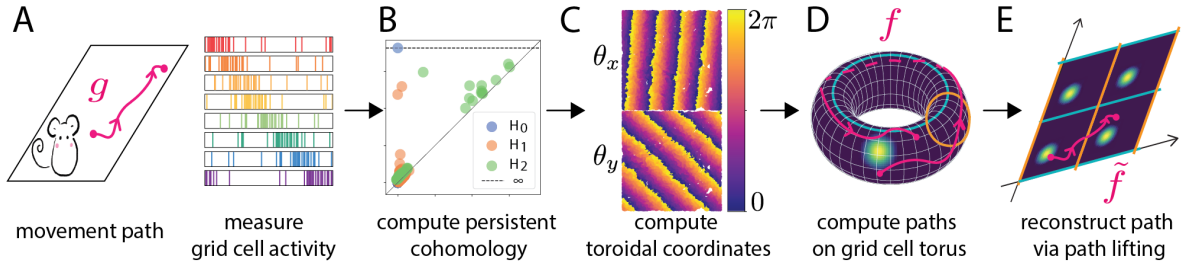


Figure 1. Constructing an internal representation of space from grid cell activity. **A.** The input data is grid cell activity collected while the mouse moves in an environment. Grid cell population activity is represented as a population vector $P(t)$ evolving over time. **B.** Persistent cohomology indicates that the population vectors are organized on a torus. **C.** Each population vector $P(t)$ is assigned toroidal coordinates (θ_x^t, θ_y^t) . Here, if the mouse is at location (x, y) at time t , we show the toroidal coordinates θ_x^t (top) and θ_y^t (bottom) by color values over location (x, y) . **D.** The toroidal coordinates form a path f on the grid cell torus. **E.** We finally lift f to a path \tilde{f} in \mathbb{R}^2 that matches the subject's movement upto an affine transformation.

From grid cell activity to path on a torus. The input is grid cell activity from a subject navigating a spatial environment, represented as a $N \times T$ matrix M , where N is the number of grid cells and T is the number of time bins. The $(i, j)^{\text{th}}$ entry represents the activity of neuron i and time bin j ². Each column of M corresponds to the population vector $P(t)$ at time t . Although these vectors live in N -dimensions, the collection $\{P(t)\}_{t=0}^T$ reside on a low-dimensional manifold called a torus [15]. Persistent (co)homology, confirms that this low-dimensional manifold has the homology of a torus: one connected component, two 1-dimensional cycles, and one 2-dimensional void (see Fig. 1B). We refer to this manifold as the *grid cell torus*.

Each population vector $P(t)$ is then parametrized by toroidal coordinates [29, 30] (*Materials and Methods*), reflecting its position on the grid cell torus (see Fig. 9). Formally, we define the map $\Theta : \{0, 1, \dots, T\} \rightarrow S^1 \times S^1$ by

$$\Theta(t) = (\theta_x^t, \theta_y^t),$$

²The entries of the matrix can be binary, with $M(i, j) = 1$ indicating that neuron i fired at time bin j and $M(i, j) = 0$ representing that the neuron i did not fire at time bin j , or non-negative real numbers, with $M(i, j)$ representing the firing rate of neuron i at time bin j .

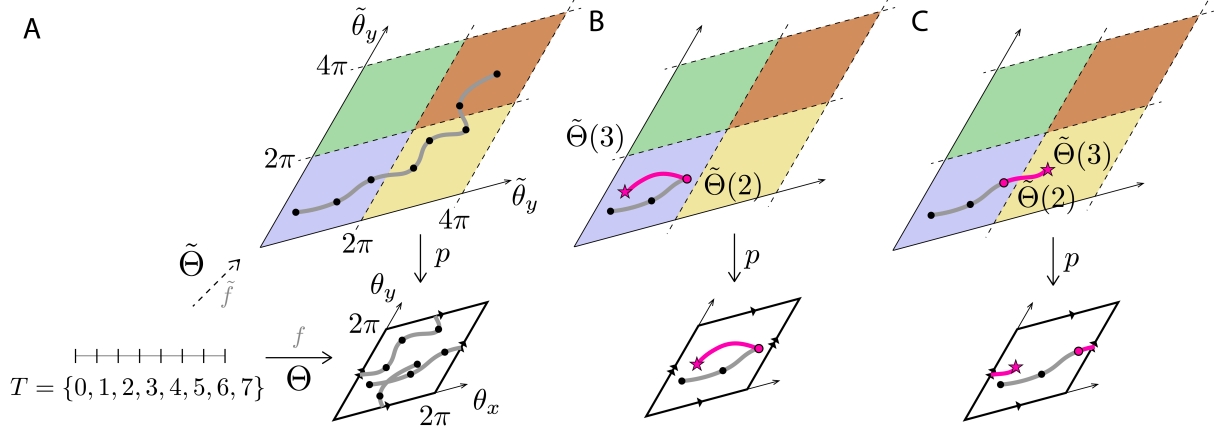


Figure 2. Lifting a discrete path Θ on the torus to a path $\tilde{\Theta}$ in \mathbb{R}^2 . **A.** Similar toroidal coordinates $\Theta(t)$ and $\Theta(t+1)$ are lifted to the same tile (no edge crossings), and dissimilar toroidal coordinates are lifted to adjacent tiles (crossing one or more torus edges). **B.** An example lifting of dissimilar toroidal coordinates $\Theta(2)$ and $\Theta(3)$, shown in circle and star in bottom panel. The first possibility is to assume that the underlying continuous path $f|_{[2,3]}$ did not cross any edges of the torus, in which case $\tilde{\Theta}(3)$ is lifted to the same tile as $\tilde{\Theta}(2)$. **C.** Second possibility is to assume that the underlying path $f|_{[2,3]}$ crossed an edge of the square torus. Here, we define $\tilde{\Theta}(3)$ to be in the tile adjacent to that of $\tilde{\Theta}(2)$.

where $\theta_x^t, \theta_y^t \in [0, 2\pi]$. Here, S^1 denotes a circle, and the torus is represented by a product of two circles, $S^1 \times S^1$. Each θ_x^t and θ_y^t represent angles on each circle. See Figure 1C.

The sequence $\{\Theta(t)\}_{t=0}^T$ form a (discrete) path on the grid cell torus (Fig. 1D).

From path on grid cell torus to a path in the plane. Once the path on torus is obtained, we finally recover the movement trajectory in \mathbb{R}^2 . Conceptually, we “unwrap” the path on the torus into \mathbb{R}^2 , which we accomplish via path liftings to covering spaces [24]. Given a covering map $p : \mathbb{R}^2 \rightarrow S^1 \times S^1$ and a continuous path $f : [0, T] \rightarrow S^1 \times S^1$ defined on the interval $[0, T]$, one can lift the path f to $\tilde{f} : [0, T] \rightarrow \mathbb{R}^2$ so that $f = p \circ \tilde{f}$, i.e., the following diagram commutes (see SI Section 1.1 for details).

$$\begin{array}{ccc} & \mathbb{R}^2 & \\ & \searrow \tilde{f} & \downarrow p \\ [0, T] & \xrightarrow{f} & S^1 \times S^1 \end{array}$$

Conceptually, the map p folds \mathbb{R}^2 into a square torus by tiling the plane into parallelograms and mapping each parallelogram to one copy of the square torus (see SI Fig. 6.). In an idealized setting where grid cell responses at the same physical location are identical, the toroidal coordinates (θ_x^*, θ_y^*) will be identical at every time point t at which the subject visits location (x, y) . In such idealized settings, the map p is defined as $p(x, y) = (\theta_x^*, \theta_y^*)$.

Here, f denotes a continuous path on the grid cell torus traced by the population vectors throughout the experiment (Fig. 2A). We treat the sequence $\{\Theta(t)\}_{t=0}^T$ as samples of the path f . The goal is to create a discrete path $\tilde{\Theta} : \{0, 1, \dots, T\} \rightarrow \mathbb{R}^2$ such that the sequence $\{\tilde{\Theta}(t)\}_{t=0}^T$ are samples of \tilde{f} . In particular, $p \circ \tilde{\Theta} = \Theta$. We perform this by lifting segments of the discrete path $\{\Theta(t)\}_{t=0}^T$ to various parallelograms of \mathbb{R}^2 . This will be done by defining $\tilde{\Theta}(t) = (\tilde{\theta}_x^t, \tilde{\theta}_y^t)$ via

$$\tilde{\theta}_x^t = \theta_x^t + 2\pi M^t \quad \text{and} \quad \tilde{\theta}_y^t = \theta_y^t + 2\pi N^t,$$

where M^t and N^t are integers specifying the tile in which the lifted point inhabits.

We define M^t and N^t inductively. First, we choose the tile closest to the origin (Fig. 2, blue tile) and define $\tilde{\Theta}(0) = \Theta(0)$ by setting $M^0 = N^0 = 0$. For consecutive time points t and $t+1$, we say the toroidal coordinates are similar if

$$(1) \quad |\theta_x^t - \theta_x^{t+1}| \leq \epsilon \quad \text{and} \quad |\theta_y^t - \theta_y^{t+1}| \leq \epsilon$$

for some proximity threshold ϵ (see *Materials and Methods* for choosing the ϵ parameter). If this pair is similar, we lift $\Theta(t+1)$ into the same tile as $\tilde{\Theta}(t)$ by setting $M^{t+1} = M^t$ and $N^{t+1} = N^t$.

If $\Theta(t)$ and $\Theta(t+1)$ fail to satisfy Equation 1, there are two possibilities for the underlying path $f|_{[t,t+1]}$. The first possibility is that the path $f|_{[t,t+1]}$ did not cross any of the edges of the torus (Fig. 2B), in which case $\tilde{\Theta}(t+1)$ should remain in the same tile as $\tilde{\Theta}(t)$. We set $M^{t+1} = M^t$ and $N^{t+1} = N^t$.

The second possibility is that $f|_{[t,t+1]}$ crossed at least one edge of the square torus (Fig. 2C), in which case $\tilde{\Theta}(t+1)$ should lie in a tile adjacent to that of $\tilde{\Theta}(t)$. This amounts to setting $M^{t+1} = M^t \pm 1$ and (or) $N^{t+1} = N^t \pm 1$ ³.

In practice, the underlying path f is unobserved, so we do not know which case applies. We therefore compare both cases and choose the lift that results in a smaller distance to $\tilde{\Theta}(t)$ for each coordinate. That is,

$$M_{t+1} = \operatorname{argmin}_{M \in \{M_t, M_t \pm 1\}} |\theta_x^t, \theta_x^t + 2\pi M|, \quad N_{t+1} = \operatorname{argmin}_{N \in \{N_t, N_t \pm 1\}} |\theta_y^t, \theta_y^t + 2\pi N|.$$

See Fig. 2 for an illustration. We repeat this process for all time points to obtain the full lifted sequence $\{\tilde{\Theta}(t)\}_{t=0}^T$. We consider $\{\tilde{\Theta}(t)\}_{t=0}^T$ as the reconstructed movement path in \mathbb{R}^2 (Fig. 2E). In the following sections, we show that this reconstructed path closely matches the subject's true trajectory up to an affine transformation. We emphasize that the subject's physical location is not used in the path reconstruction process.

2.2. Grid cell activity accurately reflects the geometry of the environment. A fundamental question is whether the proposed method can faithfully reconstruct the true movement trajectory from grid cell activity. To test this, we first consider simulated grid cell activity where the ground-truth trajectory is known.

We simulated mouse trajectories in three environments with zero, one, and two holes (Fig. 4A). Grid cell activity was generated using a continuous attractor network (CAN) model [4, 15], implemented on a 56×44 grid cell network with a shared spatial resolution. This produced

³If the subject moved quickly during time interval $[t, t+1]$, then it's possible that we need $\tilde{\Theta}(t+1)$ to be in a tile that is not adjacent to the tile containing $\tilde{\Theta}(t)$ in order for the lifted path to resemble the original movement path. Here, we assume that enough time points are observed so that this doesn't occur.

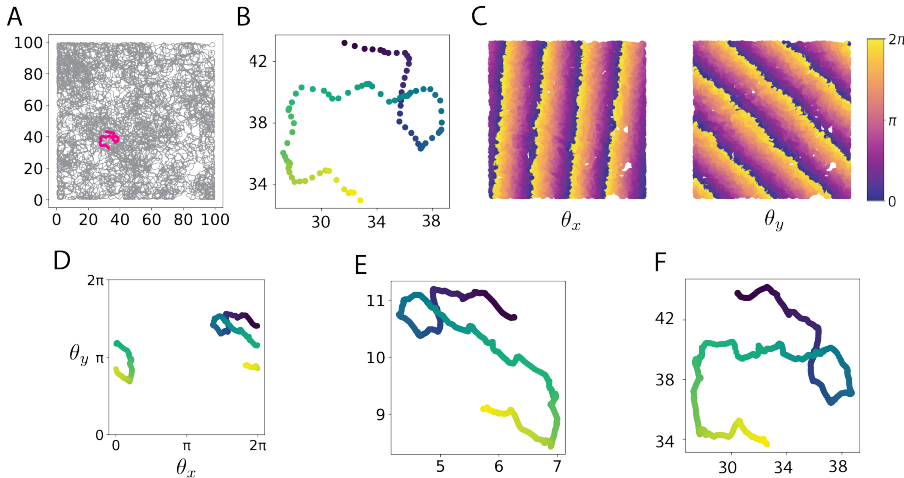


Figure 3. Illustration of path lifting on a simulated path. **A.** A simulated movement path, with a highlighted segment. **B.** Enlarged view of the highlighted segment. The color indicates that the simulated mouse moves from dark to light. **C.** Toroidal coordinates for each location on the map. The repeated values indicate that the map is large enough to require nontrivial lifting during path reconstruction. **D.** The toroidal coordinates corresponding to the path segment in panel B. **E.** The output of the reconstruction algorithm, resembling the original path in panel B. **F.** The reconstructed path, post affine transformation, recovers the original movement path in panel B.

simulated activity of 2,464 grid cells over 599,999 time bins (see *Materials and Methods*). We then applied the proposed pipeline to reconstruct the movement paths (Fig. 3).

The reconstructed trajectories preserved the global topology of the environment. Persistence diagrams computed from the reconstructed paths revealed the correct number of connected components and one-dimensional holes in the physical map (Fig. 4B). Visualizations of the reconstructed paths likewise captured the presence of holes (Fig. 4C). These results demonstrate that activity of a single-module grid cell provides sufficient information to recover topological feature of the environment.

We then investigated how well the reconstructed path resembles the geometry of the original movement path. We first aligned the reconstructed path to the ground-truth trajectory via an optimal affine transformation (*Materials and Methods*). The aligned reconstructed paths closely matched the originals, not only preserving the holes but also reflecting spatial patterns such as frequently visited regions (Fig. 4D). Quantitatively, the reconstruction error – defined as the mean Euclidean distance between the original and the aligned reconstructed path – was significantly lower than the errors from random reconstructions (z-scores: -7.5, -5.6, -8.6) (Fig. 4E), where random reconstruction error refers to the error between two randomly simulated paths in the same environment.

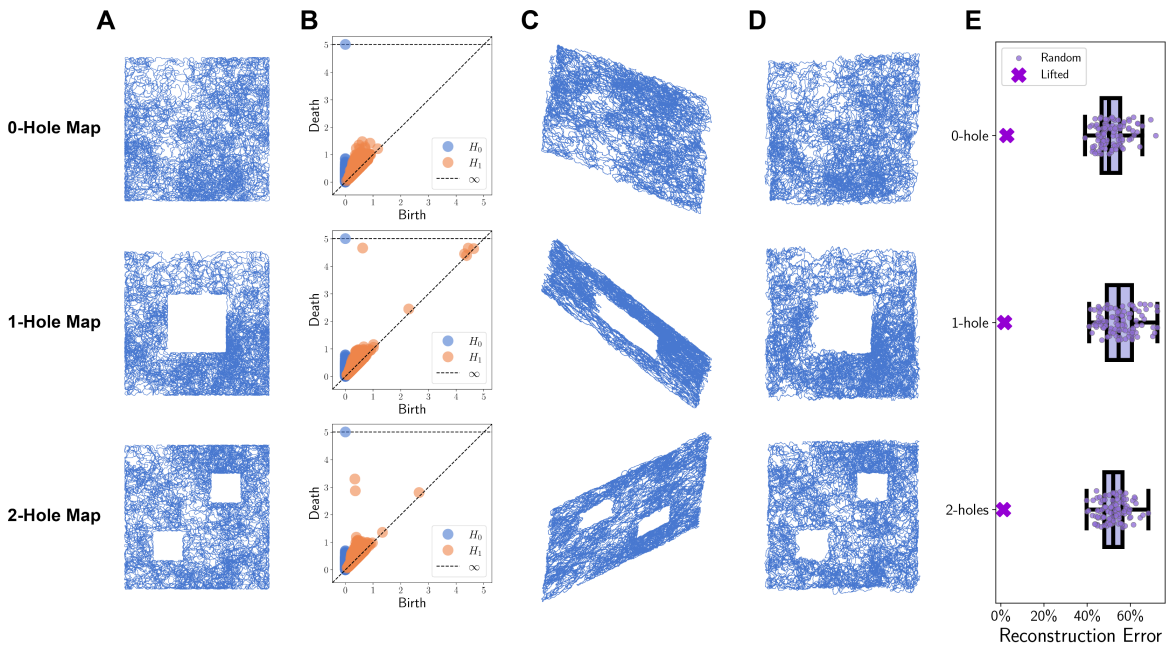


Figure 4. Path lifting on simulated grid cell activity reconstructs the original movement path. **A.** Simulated movement trajectories in environments with 0, 1, and 2 holes. **B.** The persistence diagrams computed on the reconstructed path recover the correct number of holes in the environment. **C.** Reconstructed paths from the simulation of mouse movement on maps with 0, 1, and 2 holes reflect the topology of the maps. **D.** After optimal affine alignment, the reconstructed paths resemble the original movements in panel A. **E.** Reconstruction errors between the original and reconstructed paths are significantly smaller than random baselines.

We next tested robustness to noise by introducing random spiking events, mimicking spontaneous firing. This was achieved by adding Gaussian-shaped noise events of peak height h and variance σ^2 at random time points to the simulated firing rates. The number of noise events added was controlled by a proportion parameter p (*Materials and Methods*).

When random firing is introduced to relatively small proportion of time points, for example, $p < 10\%$, the reconstructions remained highly accurate even under large noise variance σ^2 , with errors comparable to those from the original data (see Fig. 5 and Table 1). Even when the resulting firing rates look visibly very different from the original, the reconstruction errors remained small (see Fig. 5 and Table 1). However, at higher p , the toroidal structure of the

grid cell activity degraded, leading to poor or failed reconstructions (see Table 1 and SI Fig. 8). These results show that the reconstruction method is robust to moderate levels of noise but fails when spurious activity overwhelms the toroidal organization of grid cells. See SI Sections 2 and 3 for a complete collection of the reconstruction errors for the different parameter combinations.

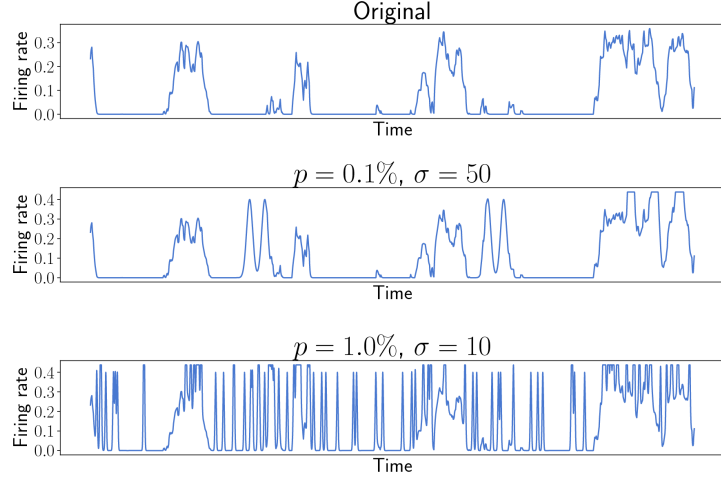


Figure 5. Example simulated grid cell firing rates with spontaneous firings that lead to low path reconstruction errors. (Top) An example simulated grid cell firing rates. (Center) Firing rates with additional spontaneous firings, generated with $h = 0.4$, $p = 0.1\%$ and $\sigma = 50$. The mean reconstruction error for such noisy firing rates is 1.975% (see Table 1). (Bottom) Firing rates with additional spontaneous firings, generated with $h = 0.4$, $p = 1\%$ and $\sigma = 10$. The mean reconstruction error is 4.319% (see Table 1).

		Standard Deviation (σ)			
		%	1	10	50
Proportion (p)	0.1 %	$1.583 \pm 0.0262(9)$	$1.645 \pm 0.0396(10)$	$1.974 \pm 0.1221(10)$	$19.683 \pm 7.2971(10)$
	0.5 %	$1.609 \pm 0.0297(10)$	$1.777 \pm 0.0346(10)$	$57.116 \pm 14.0838(10)$	$62.489 \pm 23.7991(10)$
	1 %	$1.618 \pm 0.0432(10)$	$4.319 \pm 6.2126(10)$	$97.261 \pm 60.5798(10)$	$58.523 \pm 33.0307(10)$
	5 %	$1.710 \pm 0.0869(10)$	$42.278 \pm 15.9065(10)$	N/A	N/A
	10 %	$8.855 \pm 6.6194(10)$	$66.176 \pm 28.1014(10)$	N/A	N/A

Table 1. Average reconstruction errors (%) between the original trajectory and the reconstructed paths over 10 trials. Here, the maximum height of the spontaneous firing is fixed at $h = 0.4$. The rows represent the proportion of times during which a grid cell randomly fired, and the columns represent the variance σ of the noise added. An entry of N/A indicates that the method failed to compute toroidal coordinates in all 10 trials. The numbers in parentheses represent the number trials in which path toroidal coordinates were successfully computed.

2.3. Path reconstructions recovers one-dimensional environment from grid cell activity. We applied the method to experimental data, asking whether one-dimensional trajectories can be reconstructed from real grid cell recordings. We analyzed a publicly available dataset of grid cell activity in mice navigating a 320 cm virtual build-up track [38]. Here, whenever the mouse reached the end of a track, the mouse was teleported to the start without visual discontinuity (Fig. 6A). The co-modular grid cells were identified via clustering on spectrograms (see [38] for details).

From 44 identified grid cells, the persistence diagrams confirmed a toroidal organization of population activity (Fig. 6B). While toroidal coordinates were computed using the entire

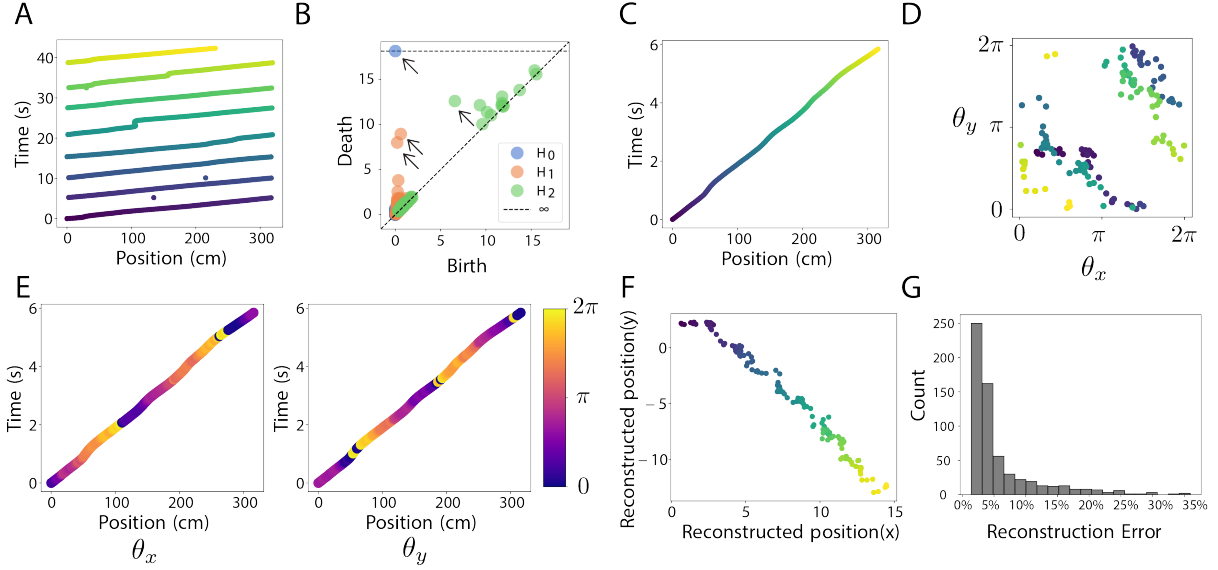


Figure 6. Path reconstruction recovers one-dimensional environment from grid cell activity. **A.** Mouse position in a 320 cm virtual build-up track; the mouse is teleported to the start upon reaching the end. **B.** The persistence diagram confirms that grid cells are organized on a torus: one connected component (H_0), two one-dimensional cycles (H_1), and one two-dimensional void (H_2). **C.** A segment of the movement path. **D.** Path on the grid cell torus corresponding to the segment in panel C. For each time point t , the corresponding toroidal coordinates θ_x and θ_y are plotted. The dark colors indicate earlier times. **E.** Toroidal coordinates visualized on the original movement path. At time point t and position x , the corresponding toroidal coordinates θ_x and θ_y are visualized via the plasma colormap. **F.** The reconstructed path resembles the one-dimensional movement of panel B. **G.** The median reconstruction error for 617 path segments was 3.6%.

experiment, path reconstructions were performed separately on each continuous run of the track, yielding 617 total runs.

For each run, the toroidal coordinates (θ_x, θ_y) cross the edges of the grid cell torus (Fig. 6D,E), indicating that the path reconstruction will involve nontrivial liftings. The reconstructed paths recovered the one-dimensional structure of the environment (see Fig. 6F and SI Fig. 9). Across all 617 runs, the median reconstruction error was 3.6% (Fig. 6G). This analysis demonstrate that one-dimensional spatial structure can be reliably decoded from experimental grid cell activity.

2.4. Local paths can be reconstructed from grid cell activity in a two-dimensional environment. Finally, we tested the method on two-dimensional experimental data that is publicly shared in [15]. Extracellular spikes from grid cells in layers II and III of MEC-parasubiculum were recorded while rats explored a square open-field arena of size $1.5m \times 1.5m$ (Fig. 7A). Six grid modules were identified by clustering. Here, we report the analysis on one of the datasets (rat R , module 1, day 2, OF).

Globally, the reconstructed path differed in overall shape from the true trajectory (Fig. 7B). However, when the analysis was restricted to shorter “local paths” (40-second intervals), the reconstructed paths were highly consistent with the original movement paths (Fig. 7E-J). For example, the reconstructed paths in Fig. 7G and J resemble the geometry of the original local paths in Fig. 7E and H, despite requiring many non-trivial lifts across torus edges (Fig. 7 F, I).

To quantify the quality of local path reconstructions, we compared reconstruction errors between the original and lifted path segments against a baseline distribution of mismatched segment pairs. Local reconstructions had significantly lower errors (mean 0.120) than the null baseline (mean 0.288, s.d. 0.089, Fig. 7K), confirmed by an independent t-test ($t(2015) = -14.5, p < 0.0001$). These results establish that while global reconstructions may deviate from the true path, local trajectories can be faithfully recovered.

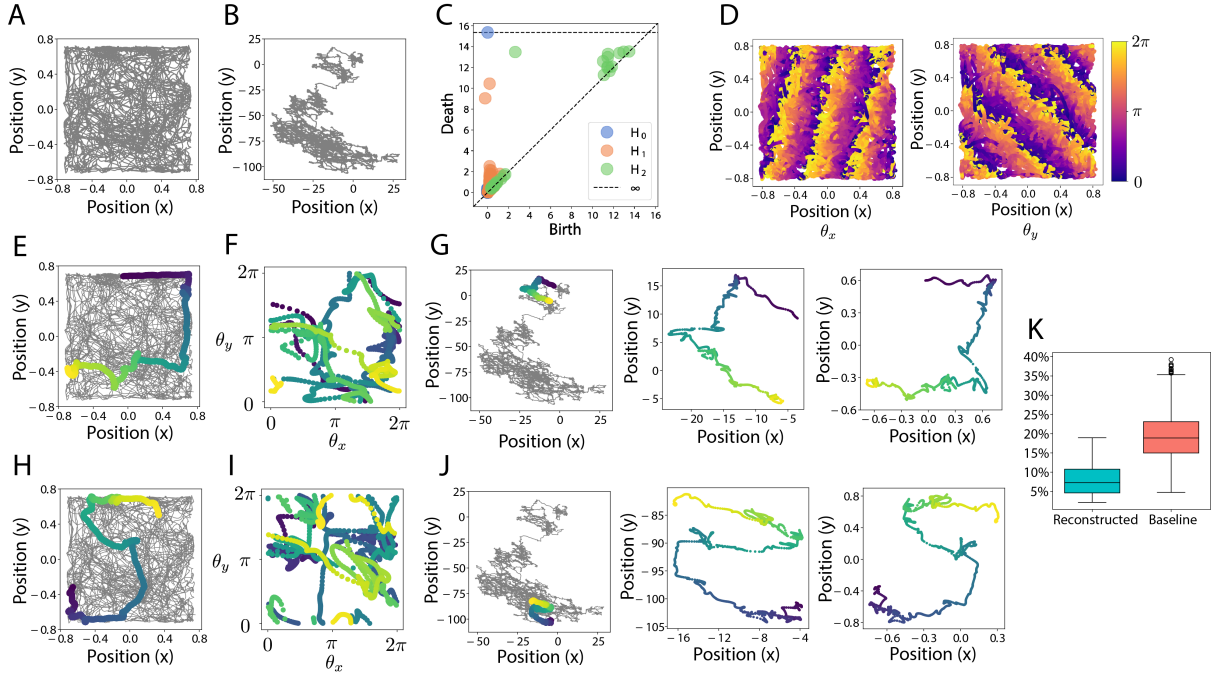


Figure 7. Reconstruction of local paths from two-dimensional experimental data [15]. **A.** The original trajectory of a rat exploring a $1.5m \times 1.5m$ open-field arena. **B.** The reconstructed global trajectory, which differs in overall shape from the original path. **C.** The persistence diagram indicates that the grid cells are organized on a torus. **D.** A visualization of the toroidal coordinates for each location. **E.** An example local path. **F.** The toroidal coordinates corresponding to panel E involve non-trivial liftings. **G.** A highlight of the reconstructed segment in panel B (left), the reconstructed path, before affine transformation (center), and after affine transformation (right). **H - J.** Another example local path and its reconstruction. **K.** Distribution of reconstruction errors: pairs of original local paths and reconstructed paths (left) show significantly smaller errors than baseline consisting of mismatched local paths (right) ($t(2015) = -14.5, p < 0.0001$).

Several factors can contribute to the discrepancy between local and global path reconstructions. First, noise in the toroidal coordinates can distort lifted path (compare Fig. 7D to Fig. 3C). Second, when the time points are sparse or the animal moves quickly, two types of lifting errors can occur: toroidal coordinates $\Theta(t)$ and $\Theta(t+1)$ that should be lifted to the same tile may be lifted to different tiles (see Fig. 8A), or coordinates $\Theta(t)$ and $\Theta(t+1)$ that should be lifted to distinct tiles may end up lifting to the same tile (see Fig. 8B). Accumulated errors of this type can cause large-scale distortions in the global path reconstruction.

3. DISCUSSION

In this study, we introduced and validated a topological framework for decoding spatial trajectories from grid cell population activity. By identifying toroidal coordinates through persistent cohomology and lifting paths from the torus to the plane, we effectively reconstruct movement trajectories up to an affine transformation. This approach decodes spatial trajectories without access to external positional cues or knowledge of grid phases, offering a new computational perspective on spatial representation of the grid cell system. Our results show that the toroidal organization of grid cell activity is not merely a descriptive feature but can be functionally leveraged to recover spatial information.

The proposed method complements previous decoding approaches in that it only requires the activity of a single grid module (as opposed to multiple grid modules) [21, 32] and that it doesn't involve any training process. Furthermore, the method doesn't require any phase information of the grid modules, enhancing the applicability of the method.

In order for the method to reconstruct paths accurately, several assumptions must be met. The presented method requires that the grid cells are recorded for a sufficiently long time so

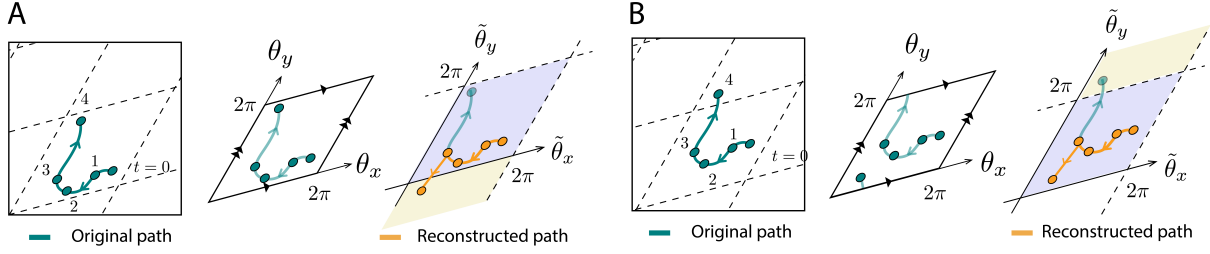


Figure 8. Two possible errors in path reconstruction arising from sparsity of time points. **A.** The first type of error occurs when two consecutive toroidal coordinates are lifted to two distinct tiles when they should be lifted to a single tile. (Left) Original movement path. Circles indicate the location at select time points. (Center) The corresponding toroidal coordinates. (Right) The algorithm lifts the toroidal coordinates $\Theta(0), \dots, \Theta(3)$ to the blue tile. Because θ_y^3 and θ_y^4 are dissimilar, $\Theta(4)$ is in a different tile, shown in yellow. The resulting reconstructed path (orange) deviates from the original path (green). **B.** The second type of error occurs when two consecutive toroidal coordinates are lifted to the same tile when they should be lifted to different tiles. Here, the toroidal coordinates θ_y^3 and θ_y^4 have a small enough difference so the algorithm lifts $\Theta(3)$ and $\Theta(4)$ to the same tile. Again, the reconstructed path (orange) deviates from the original (green).

that the toroidal structure of the population vectors become clear. Furthermore, accurate path reconstruction depends on sufficiently dense temporal sampling. As discussed in Fig. 8, having insufficient timepoints or the subject moving quickly between two timepoints can lead to poor lifting. On the other hand, including too many timepoints can lead to slow computation, especially when computing the toroidal coordinates. In particular, the analysis of two-dimensional experimental data involves a preprocessing that selects the relevant timepoints. Such preprocessing must be done in a manner that preserves the toroidal structure of grid cells.

There are several directions for future research. Incorporating interpolation and probabilistic inference during path lifting could improve robustness to sparse or noisy data. Combining grid modules of different phases may provide a more comprehensive and precise decoding framework. Future research should also examine how the toroidal organization of grid cells integrate with other spatially tuned cell populations such as place cells to support path integration and spatial navigation. Beyond neuroscience, the method offers new perspectives on sparse coding and representation, with potential applications in robotics, brain-computer interfaces, and agent-based navigation systems.

4. MATERIALS AND METHODS

4.1. Simulation of grid cells.

4.1.1. Simulated Mice Trajectory.

A two-dimensional random walk simulation was developed to model the exploratory behavior of mice within a bounded environment (100×100). The environment was defined by spatial boundaries and obstacle parameters, including the sizes and positions of holes. A mouse agent was initially placed at a randomly selected valid location within these boundaries. At each time step, candidate positions were computed within an angular window of $\pm 75^\circ$ relative to the current heading. A step size is randomly drawn up to a predefined maximum, and candidate positions are generated by adding a scaled directional vector to the current position. Only positions that remained within the environment and avoided designated holes were accepted. If no valid candidate position was available, the agent remained stationary for that time step and subsequently adopted a new random heading from the full 360° range. Repeated iterations of this process produced a random trajectory that models the exploratory behavior of mice.

4.1.2. Grid Cell Simulation with CAN Model.

Grid cell activities were simulated using a noiseless CAN model, following [4, 15]. Specifically, we use the same model and parameters as described in [15]. We refer the reader to [15] for details.

4.1.3. *Simulation of grid cells with additional spontaneous firings.* To emulate the random firing of grid cells, we incorporated one-dimensional Gaussian noise into the simulated grid cell firing rates. Given a simulated firing rate $r(t)$ with $t \in [0, T]$, we modify $r(t)$ by adding one-dimensional Gaussian functions $g_{h,\sigma}(t)$ centered at some random value in $[0, T]$, with peak height h and variance σ^2 . Letting $r_{\max} = \max_t r(t)$, the maximum firing rate in the simulated data, we construct a noisy firing rate by

$$r^*(t) = \min \left\{ r(t) + \sum_i g_{\sigma,h}(t), r_{\max} \right\}.$$

We clip the simulated firing rate so that $r^*(t)$ doesn't exceed the maximum firing rate r_{\max} from the original simulation. Here, the number of Gaussian functions added can vary, and the number is determined as some proportion p of T .

For computational efficiency, a fast approximation routine precomputes a truncated Gaussian curve by identifying the index at which the noise amplitude falls below a specified threshold of 1e-4, thereby limiting the range over which noise is applied.

4.2. Topological features.

4.2.1. *Persistent cohomology.* Persistent (co)homology is a tool in topological data analysis that can be used to identify structural features in neural manifolds. Here, it is used firstly to verify that the grid cells' population activity is organized in a torus and secondly to compute the toroidal coordinates of each population vector. Let $P = \{P_1, \dots, P_N\}$ denote the collection of population vectors at N time points. We compute the $N \times N$ pairwise dissimilarity matrix D_P . Let $\{\delta_i\}_{i=1}^m$ be a collection of parameters. Given a parameter δ , we construct a Vietoris-Rips complex $R_\delta(P)$ whose vertex set is N and has an n -simplex $[v_0, \dots, v_n]$ precisely when all pairwise dissimilarity among the listed elements is at most δ_k . We then obtain a filtration of Vietoris-Rips complexes

$$R_{\delta_1}(P) \subseteq R_{\delta_2}(P) \subseteq \dots \subseteq R_{\delta_m}(P).$$

Computing (co)homology in dimensions 0, 1, and 2 with a field coefficient, we obtain a sequence of vector spaces summarizing the connected components, circular features, and voids in each simplicial complex at each parameter. The birth and death of these topological features are summarized in a persistence diagram. A topological feature born at parameter b that dies at parameter d is represented by a point in the plane with coordinates (b, d) . Ripser [2, 36] was used for persistent cohomology computations.

4.2.2. Circular coordinates.

Given a point cloud P that is arranged in a circular fashion, *circular coordinates* is a parametrization of P using a circle-valued map $f : P \rightarrow S^1$, where S^1 refers to a circle. In practice, the range of the circular coordinates will be the angles $[0, 2\pi)$, considered as a circle after identifying 0 and 2π . Originally presented in [30], the construction is motivated by the fact that there is a bijection between the equivalence classes of continuous maps from a CW complex X to the circle S^1 and the cohomology of X with integer coefficients

$$[X, S^1] = H^1(X; \mathbb{Z}).$$

Given a point cloud P , persistent cohomology is used to fix a Vietoris-Rips complex $R_\delta(P)$ such that there is a nontrivial circular structure. Then a generator $[\eta] \in H^1(R_\delta(P); \mathbb{Z})$ is used to assign circular coordinates to each point of P . See [30] for details.

4.2.3. *Toroidal coordinates.* Toroidal coordinates parameterize points on a torus. Since the torus $S^1 \times S^1$ is a product of two circles, any point on the torus can be parametrized using two circular coordinates as (θ_x, θ_y) , where $\theta_x, \theta_y \in [0, 2\pi)$ (Fig. 9).

When using the original circular coordinates algorithm, one can end up with two circle-valued maps that are “geometrically correlated.” The *toroidal coordinates algorithm* [29] addresses this issue and returns circular coordinates that are geometrically “decorrelated.” In this work, we use both methods. In the simulated data, we computed the toroidal coordinates using DREiMac [27]. For the experimental data, we used the “cohomological decoding” described in [15], which

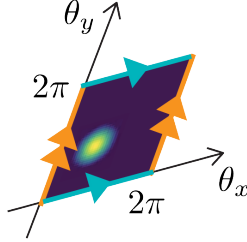


Figure 9. Toroidal coordinates parametrizes points on the torus via (θ_x, θ_y) , where $\theta_x, \theta_y \in [0, 2\pi)$.

adapts the original circular coordinates algorithm. Instead of computing the toroidal coordinates for every population vector, the method computes the toroidal coordinates for a reduced subset of 1,200 population vectors and interpolates to the rest, thereby speeding up the computation. We refer the reader to the methods section in [15] for details.

4.3. Path lifting.

4.3.1. Aligning paths via affine transformation.

An affine transformation is a linear mapping that preserves points, straight lines, and planes under rotation, translation, and scaling. It can be expressed as a linear transformation (matrix multiplication) followed by a translation (vector addition). For a given 2D vector $X = \begin{bmatrix} x \\ y \end{bmatrix}$, we define a transformation matrix

$$M = \begin{bmatrix} A & B \end{bmatrix} = \begin{bmatrix} a_{00} & a_{01} & b_{00} \\ a_{10} & a_{11} & b_{10} \end{bmatrix},$$

such that

$$T = A \cdot X + B = \begin{bmatrix} a_{00}x + a_{01}y + b_{00} \\ a_{10}x + a_{11}y + b_{10} \end{bmatrix}.$$

Using the `estimateAffine2D` function from the OpenCV package [3], we derived the optimal affine transformation matrix that maps the lifted coordinates to the original trajectory. This transformation is then applied to the entire lifted path, aligning it with the original space and allowing for subsequent calculation of the reconstruction error.

4.3.2. Reconstruction error. Given a discrete path $f(t)$ and a reconstructed path $\tilde{\Theta}(t)$, where $t = \{0, 1, \dots, T\}$, we quantify their dissimilarity as follows. We first find an optimal affine transformation to align $\tilde{\Theta}$ to f . Let $\tilde{\Theta}^*$ denote the transformed discrete path. We define the reconstruction error to be the average Euclidean distance between points on f and $\tilde{\Theta}^*$:

$$\frac{1}{S} \cdot \frac{1}{T+1} \sum_{t=0}^T \|f(t), \tilde{\Theta}^*(t)\|.$$

Here, S is a normalization factor that allows us to interpret the error as a percentage of the size of the physical environment. In the simulation study, $S = 100$, which is the length and width of the map. In the one-dimensional experimental study, $S = 320$, which is the length of the build-up track. In the two-dimensional experimental study, $S = 1.5$, which is the length and width of the physical environment for each segment. A lower reconstruction error indicates a higher degree of alignment between the original path and the reconstructed path.

4.3.3. *Proximity parameter selection.* The parameter ϵ identifies potential time points at which the toroidal coordinates have crossed the edge of a square torus. To select ϵ , we first compute the maximal coordinate difference $cd^t = \max\{|\theta_x^t - \theta_x^{t+1}|, |\theta_y^t - \theta_y^{t+1}|\}$ for every time point t . We then observe the histogram of the maximal coordinate differences, which ranges from 0 to 2π . The values are highly concentrated near 0 and 2π .

For most time points, the coordinate difference will be very small. In order to exclude the maximal coordinate differences near 0, we consider the coordinate differences in the range $[2, 2\pi]$. We then reverse the order of the coordinate differences (that is, we consider $2\pi - cd^t$), consider the cumulative distribution function (CDF) of the order-reversed coordinate differences, and select ϵ to be the value at which the CDF first exceeds a predetermined threshold, typically set at $\alpha = 0.99$. See SI Fig. 7 for example histograms and ϵ parameter selection.

4.4. **Code Availability.** Code can be found at the following Github repository <https://github.com/irishryoon/GridPathLifting>. For simulations, we modified the code shared in <https://github.com/erikher/GridCellTorus>.

4.5. **Data Availability.** All experimental data in this manuscript are from publicly available datasets. The one-dimensional movement dataset [38] can be found at <https://data.mendeley.com/datasets/rGTK6jygjc/1>. We report the analysis on dataset “N2_200203_buildup_track.mat.” The two-dimensional open field movement dataset [15] can be found at https://figshare.com/articles/dataset/Toroidal_topology_of_population_activity_in_grid_cells/16764508. Both datasets have been made public by the authors of the corresponding publications.

REFERENCES

- [1] C Barry and D Bush. *From A to Z: a potential role for grid cells in spatial navigation.* 523 *Neural Syst.* 2012.
- [2] Ulrich Bauer. “Ripser: efficient computation of Vietoris–Rips persistence barcodes”. In: *Journal of Applied and Computational Topology* 5.3 (2021), pp. 391–423.
- [3] G. Bradski. “The OpenCV Library”. In: *Dr. Dobb’s Journal of Software Tools* (2000).
- [4] Yoram Burak and Ila R Fiete. “Accurate path integration in continuous attractor network models of grid cells”. In: *PLoS computational biology* 5.2 (2009), e1000291.
- [5] Daniel Bush, Caswell Barry, Daniel Manson, and Neil Burgess. “Using grid cells for navigation”. In: *Neuron* 87.3 (2015), pp. 507–520.
- [6] Gunnar Carlsson. “Topology and Data”. In: *Bulletin of The American Mathematical Society - BULL AMER MATH SOC* 46 (Apr. 2009), pp. 255–308. DOI: [10.1090/S0273-0979-09-01249-X](https://doi.org/10.1090/S0273-0979-09-01249-X).
- [7] Rishidev Chaudhuri, Berk Gerçek, Biraj Pandey, Adrien Peyrache, and Ila Fiete. “The intrinsic attractor manifold and population dynamics of a canonical cognitive circuit across waking and sleep”. en. In: *Nature Neuroscience* 22.9 (Sept. 2019). Number: 9 Publisher: Nature Publishing Group, pp. 1512–1520. ISSN: 1546-1726. DOI: [10.1038/s41593-019-0460-x](https://doi.org/10.1038/s41593-019-0460-x).
- [8] Suogui Dang, Yining Wu, Rui Yan, and Huajin Tang. “Why grid cells function as a metric for space”. In: *Neural Networks* 142 (2021), pp. 128–137.
- [9] Herbert Edelsbrunner, John Harer, et al. “Persistent homology-a survey”. In: *Contemporary mathematics* 453.26 (2008), pp. 257–282.
- [10] Edelsbrunner, Letscher, and Zomorodian. “Topological persistence and simplification”. In: *Discrete & computational geometry* 28 (2002), pp. 511–533.
- [11] Uğur M Erdem and Michael Hasselmo. “A goal-directed spatial navigation model using forward trajectory planning based on grid cells”. In: *European Journal of Neuroscience* 35.6 (2012), pp. 916–931.
- [12] Ila R. Fiete, Yoram Burak, and Ted Brookings. “What Grid Cells Convey about Rat Location”. en. In: *Journal of Neuroscience* 28.27 (July 2008). Publisher: Society for Neuroscience Section: Articles, pp. 6858–6871. ISSN: 0270-6474, 1529-2401. DOI: [10.1523/JNEUROSCI.5684-07.2008](https://doi.org/10.1523/JNEUROSCI.5684-07.2008).
- [13] Markus Frey, Sander Tanni, Catherine Perrodin, Alice O’Leary, Matthias Nau, Jack Kelly, Andrea Banino, Christian F. Doeller, and Caswell Barry. *Deepinsight: a general framework for interpreting wide-band neural activity*. en. Pages: 871848 Section: New Results. Dec. 2019. DOI: [10.1101/871848](https://doi.org/10.1101/871848).
- [14] Mark C Fuhs and David S Touretzky. “A spin glass model of path integration in rat medial entorhinal cortex”. In: *Journal of Neuroscience* 26.16 (2006), pp. 4266–4276.
- [15] Richard J. Gardner, Erik Hermansen, Marius Pachitariu, Yoram Burak, Nils A. Baas, Benjamin A. Dunn, May-Britt Moser, and Edvard I. Moser. “Toroidal topology of population activity in grid cells”. In: *Nature* 602.7895 (Feb. 2022). Publisher: Nature Publishing Group, pp. 123–128. ISSN: 1476-4687. DOI: [10.1038/s41586-021-04268-7](https://doi.org/10.1038/s41586-021-04268-7).
- [16] Robert Ghrist. “Barcodes: the persistent topology of data”. In: *Bulletin of the American Mathematical Society* 45.1 (2008), pp. 61–75.
- [17] Torkel Hafting, Marianne Fyhn, Sturla Molden, May-Britt Moser, and Edvard I Moser. “Microstructure of a spatial map in the entorhinal cortex”. In: *Nature* 436.7052 (2005), pp. 801–806.
- [18] D. H. Hubel and T. N. Wiesel. “Receptive fields and functional architecture of monkey striate cortex”. eng. In: *The Journal of Physiology* 195.1 (Mar. 1968), pp. 215–243. ISSN: 0022-3751. DOI: [10.1113/jphysiol.1968.sp008455](https://doi.org/10.1113/jphysiol.1968.sp008455).
- [19] Jesse A Livezey and Joshua I Glaser. “Deep learning approaches for neural decoding across architectures and recording modalities”. In: *Briefings in Bioinformatics* 22.2 (Dec. 2020). eprint: <https://academic.oup.com/bib/article-pdf/22/2/1577/36654842/bbaa355.pdf>, pp. 1577–1591. ISSN: 1477-4054. DOI: [10.1093/bib/bbaa355](https://doi.org/10.1093/bib/bbaa355).

[20] Cécile Masson and Benoît Girard. “Decoding the Grid Cells for Metric Navigation Using the Residue Numeral System”. In: *Advances in Cognitive Neurodynamics (II)*. Ed. by Rubin Wang and Fanji Gu. Dordrecht: Springer Netherlands, 2011, pp. 459–464. ISBN: 978-90-481-9695-1.

[21] Alexander Mathis, Andreas VM Herz, and Martin Stemmler. “Optimal population codes for space: grid cells outperform place cells”. In: *Neural computation* 24.9 (2012), pp. 2280–2317.

[22] Bruce L McNaughton, Francesco P Battaglia, Ole Jensen, Edvard I Moser, and May-Britt Moser. “Path integration and the neural basis of the ‘cognitive map’”. In: *Nature Reviews Neuroscience* 7.8 (2006), pp. 663–678.

[23] Edward C. Mitchell, Brittany Story, David Boothe, Piotr J. Franaszczuk, and Vasileios Maroulas. “A topological deep learning framework for neural spike decoding”. English. In: *Biophysical Journal* 123.17 (Sept. 2024). Publisher: Elsevier, pp. 2781–2789. ISSN: 0006-3495, 1542-0086. DOI: [10.1016/j.bpj.2024.01.025](https://doi.org/10.1016/j.bpj.2024.01.025).

[24] J. Munkres. *Topology*. Pearson Modern Classics for Advanced Mathematics Series. Pearson, 2017. ISBN: 9780134689517.

[25] John O’Keefe. “Place units in the hippocampus of the freely moving rat”. In: *Experimental Neurology* 51.1 (Jan. 1976), pp. 78–109. ISSN: 0014-4886. DOI: [10.1016/0014-4886\(76\)90055-8](https://doi.org/10.1016/0014-4886(76)90055-8).

[26] Jing-Jie Peng, Beate Throm, Maryam Najafian Jazi, Ting-Yun Yen, Hannah Monyer, and Kevin Allen. *Grid cells perform path integration in multiple reference frames during self-motion-based navigation*. en. Pages: 2023.12.21.572857 Section: New Results. Dec. 2023. DOI: [10.1101/2023.12.21.572857](https://doi.org/10.1101/2023.12.21.572857).

[27] Jose A. Perea, Luis Scoccola, and Christopher J. Tralie. “DREiMac: Dimensionality Reduction with Eilenberg-MacLane Coordinates”. In: *Journal of Open Source Software* 8.91 (2023), p. 5791. DOI: [10.21105/joss.05791](https://doi.org/10.21105/joss.05791).

[28] Erik Rybakken, Nils Baas, and Benjamin Dunn. “Decoding of Neural Data Using Cohomological Feature Extraction”. In: *Neural Computation* 31.1 (Jan. 2019), pp. 68–93. ISSN: 0899-7667. DOI: [10.1162/neco_a_01150](https://doi.org/10.1162/neco_a_01150).

[29] Luis Scoccola, Hitesh Gakhar, Johnathan Bush, Nikolas Schonsheck, Tatum Rask, Ling Zhou, and Jose A. Perea. “Toroidal Coordinates: Decorrelating Circular Coordinates with Lattice Reduction”. In: *LIPICS, Volume 258, SoCG 2023* 258 (2023). In collab. with Erin W. Chambers and Joachim Gudmundsson. Artwork Size: 20 pages, 6894838 bytes ISBN: 9783959772730 Medium: application/pdf Publisher: Schloss Dagstuhl – Leibniz-Zentrum für Informatik, 57:1–57:20. ISSN: 1868-8969. DOI: [10.4230/LIPICS.SOCG.2023.57](https://doi.org/10.4230/LIPICS.SOCG.2023.57).

[30] Vin de Silva, Dmitriy Morozov, and Mikael Vejdemo-Johansson. “Persistent Cohomology and Circular Coordinates”. en. In: *Discrete & Computational Geometry* 45.4 (June 2011), pp. 737–759. ISSN: 1432-0444. DOI: [10.1007/s00454-011-9344-x](https://doi.org/10.1007/s00454-011-9344-x).

[31] Trygve Solstad, Edvard I Moser, and Gaute T Einevoll. “From grid cells to place cells: a mathematical model”. In: *Hippocampus* 16.12 (2006), pp. 1026–1031.

[32] Martin Stemmler, Alexander Mathis, and Andreas VM Herz. “Connecting multiple spatial scales to decode the population activity of grid cells”. In: *Science Advances* 1.11 (2015), e1500816.

[33] Hong Sun and Tian-Ren Yao. “A neural-like network approach to residue-to-decimal conversion”. In: *Proceedings of 1994 IEEE International Conference on Neural Networks (ICNN’94)*. Vol. 6. June 1994, 3883–3887 vol.6. DOI: [10.1109/ICNN.1994.374831](https://doi.org/10.1109/ICNN.1994.374831).

[34] Ardi Tampuu, Tambet Matiisen, H. Freyja Ólafsdóttir, Caswell Barry, and Raul Vicente. “Efficient neural decoding of self-location with a deep recurrent network”. en. In: *PLOS Computational Biology* 15.2 (Feb. 2019). Publisher: Public Library of Science, e1006822. ISSN: 1553-7358. DOI: [10.1371/journal.pcbi.1006822](https://doi.org/10.1371/journal.pcbi.1006822).

[35] Jeffrey S Taube, Robert U Muller, and James B Ranck. “Head-direction cells recorded from the postsubiculum in freely moving rats. I. Description and quantitative analysis”. In: *Journal of Neuroscience* 10.2 (1990), pp. 420–435.

- [36] Christopher Tralie, Nathaniel Saul, and Rann Bar-On. “Ripser. py: A lean persistent homology library for python”. In: *Journal of Open Source Software* 3.29 (2018), p. 925.
- [37] Vincent Villette, Arnaud Malvache, Thomas Tressard, Nathalie Dupuy, and Rosa Cossart. “Internally Recurring Hippocampal Sequences as a Population Template of Spatiotemporal Information”. eng. In: *Neuron* 88.2 (Oct. 2015), pp. 357–366. ISSN: 1097-4199. DOI: [10.1016/j.neuron.2015.09.052](https://doi.org/10.1016/j.neuron.2015.09.052).
- [38] John H Wen, Ben Sorscher, Emily A Aery Jones, Surya Ganguli, and Lisa M Giocomo. “One-shot entorhinal maps enable flexible navigation in novel environments”. In: *Nature* 635.8040 (2024), pp. 943–950.
- [39] Zishen Xu, Wei Wu, Shawn S. Winter, Max L. Mehlman, William N. Butler, Christine M. Simmons, Ryan E. Harvey, Laura E. Berkowitz, Yang Chen, Jeffrey S. Taube, Aaron A. Wilber, and Benjamin J. Clark. “A Comparison of Neural Decoding Methods and Population Coding Across Thalamo-Cortical Head Direction Cells”. English. In: *Frontiers in Neural Circuits* 13 (Dec. 2019). Publisher: Frontiers. ISSN: 1662-5110. DOI: [10.3389/fncir.2019.00075](https://doi.org/10.3389/fncir.2019.00075).
- [40] Yuansheng Zhou, Brian H. Smith, and Tatyana O. Sharpee. “Hyperbolic geometry of the olfactory space”. In: *Science Advances* 4.8 (Aug. 2018). Publisher: American Association for the Advancement of Science, eaaq1458. DOI: [10.1126/sciadv.aaq1458](https://doi.org/10.1126/sciadv.aaq1458).

APPENDIX A. SUPPLEMENTARY INFORMATION

A.1. Mathematical Preliminaries.

A.1.1. *Lifting paths on torus to paths in \mathbb{R}^2 .* Given a topological space X , a path in X is a continuous map $f : I \rightarrow X$, where $I = [0, 1]$ denotes the unit interval. If one considers $t \in [0, 1]$ as representing time, then $f(t)$ specifies the location of an object in X at time t .

In this work, we are concerned with lifting paths on a torus to paths in \mathbb{R}^2 . Recall that S^1 represents a circle, and that $S^1 \times S^1$ represents a torus. Let $f : I \rightarrow S^1 \times S^1$ be a path on the torus, and let $p : \mathbb{R}^2 \rightarrow S^1 \times S^1$ be a covering of a torus. For example, $p : \mathbb{R}^2 \rightarrow S^1 \times S^1$ defined by

$$(2) \quad p(x, y) = ((\cos 2\pi x, \sin 2\pi x), (\cos 2\pi y, \sin 2\pi y))$$

is a valid covering of a torus. Note that $(\cos 2\pi x, \sin 2\pi x)$ and $(\cos 2\pi y, \sin 2\pi y)$ each specify points in S^1 .

The following lemma states that any path on a torus can be lifted to a path in \mathbb{R}^2 .

Lemma 1. (Lemma 54.2 [24], modified) *The path $f : I \rightarrow S^1 \times S^1$ can be lifted to a path $\tilde{f} : I \rightarrow \mathbb{R}^2$ such that the following diagram commutes.*

$$\begin{array}{ccc} & \mathbb{R}^2 & \\ & \downarrow p & \\ I & \xrightarrow{f} & S^1 \times S^1 \\ & \nearrow \tilde{f} & \end{array}$$

Furthermore, given a $b_0 = f(0) \in S^1 \times S^1$ and $e_0 \in p^{-1}(b_0)$, the lifted path \tilde{f} with $\tilde{f}(0) = e_0$ is unique.

A constructive proof can be found in [24]. Here, we illustrate the construction of \tilde{f} in a simple example. Let $p : \mathbb{R}^2 \rightarrow S^1 \times S^1$ the covering map from Equation 2. We construct \tilde{f} in pieces.

Let U_1, \dots, U_4 be open sets covering the torus (Fig. SI-1A). Note that for any $U \in \{U_1, \dots, U_4\}$, the preimage $p^{-1}(U)$ consists of infinitely-many homeomorphic copies of U in \mathbb{R}^2 (Fig. SI-1B). Each copy of U in $p^{-1}(U)$ is called a *slice*.

We then partition $I = [0, 1]$ into segments $0 = s_0 < s_1 < \dots < s_4 = 1$ so that f maps each segment $[s_i, s_{i+1}]$ into one of U_1, \dots, U_4 (Figure SI-1C). Without loss of generality, assume $f(0)$ lies in U_1 . We choose some slice, let's say V_1 , of U_1 . We let $\tilde{f}(0)$ be the unique point in V_1 that maps to $f(0)$ via p . We then define \tilde{f} on $[0, s_1]$ to be the unique path in $V_1 \subset \mathbb{R}^2$ that maps to $f|_{[0, s_1]}$ via p .

To define \tilde{f} on $[s_1, s_2]$, note that $f(s_1)$ lives in both U_1 and U_2 . Among the slices $p^{-1}(U_2)$ of U_2 , there exists a unique slice, say V_2 of U_2 where $\tilde{f}(s_1) \in V_2$. We then define \tilde{f} on $[s_1, s_2]$ to be the unique path in $V_2 \subset \mathbb{R}^2$ that maps to $f|_{[s_1, s_2]}$ via p .

We continue this procedure until we define \tilde{f} on the entire interval $[0, 1]$. By construction, $p \circ \tilde{f} = f$.

A.1.2. *Persistent homology.* We provide a brief description of simplicial homology (with field coefficients) and persistent homology.

Simplicial Complexes and Simplicial Homology

An (*abstract*) *simplicial complex* $K = (V, F)$ is a combinatorial structure built from a set of vertices V . It consists of simplices, where a simplex is an unordered subset of V . A collection of $n + 1$ elements in V , for example, (v_0, \dots, v_n) , is called an n -simplex. Concretely, a single vertex is a 0-simplex, the collection (v_0, v_1) is a 1-simplex, and (v_0, v_1, v_2) is a 2-simplex. The collection of simplices F must satisfy the following: given a simplex $\sigma \in F$, all of its non-empty subsets must also be in F .

In this paper, the homology of a simplicial complex is computed with field coefficients \mathbb{F} . Therefore, all homology computations are done in the context of vector spaces and linear maps.

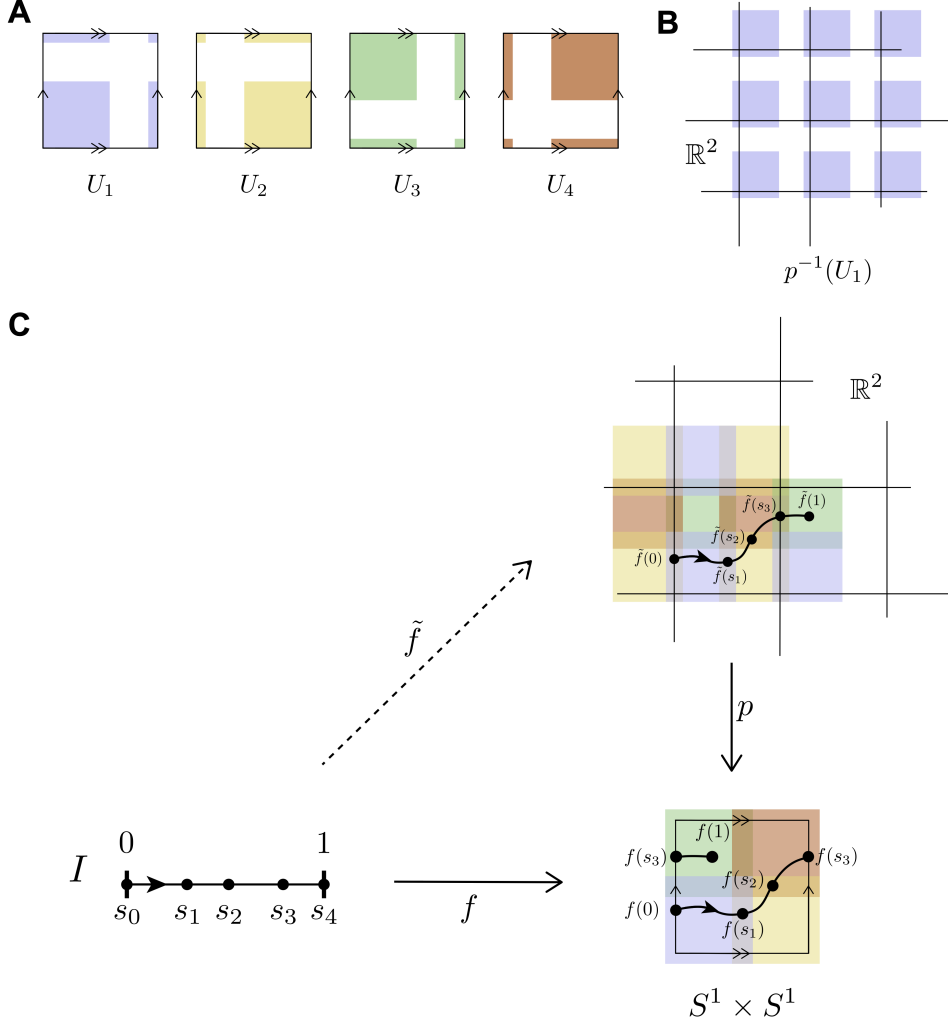


Figure SI-1. Lifting a path f on torus to a path \tilde{f} in \mathbb{R}^2 . **A.** The open cover $\{U_1, \dots, U_4\}$ of the torus. **B.** The preimage $p^{-1}(U_1)$ consist of homeomorphic copies of U_1 in \mathbb{R}^2 . **C.** The lifted path \tilde{f} is constructed piece-by-piece.

To study the topology of K , we work with *chains*, which are formal linear combinations of simplices. More precisely, if F_n denotes the number of n -simplices in a complex K , then the vector space of n -chains is

$$C_n(K) = \left\{ \sum_{i=1}^{F_n} c_i \sigma_i^n \mid c_i \in \mathbb{F}, \sigma_i^n \in K \right\}.$$

The *boundary homomorphism* $\partial_n : C_n(K) \rightarrow C_{n-1}(K)$ is constructed as follows. For an n -simplex $\sigma = (v_0, \dots, v_n)$, the boundary is defined as

$$\partial_n(\sigma) = \sum_{i=0}^n (-1)^i (v_0, \dots, \hat{v}_i, \dots, v_n),$$

where the notation \hat{v}_i means that the vertex v_i has been omitted. This map is then extended linearly to all of $C_n(K)$. We then obtain the following

$$\cdots \rightarrow C_{n+1}(K) \xrightarrow{\partial_{n+1}} C_n(K) \xrightarrow{\partial_n} C_{n-1}(K) \rightarrow \cdots \rightarrow C_0(K) \rightarrow 0,$$

which is a sequence of vector spaces and linear maps. The boundary homomorphisms satisfy the key property that $\partial_n \circ \partial_{n+1} = 0$ for all n .

This property ensures that $\text{im } \partial_{n+1} \subseteq \ker \partial_n$. Elements in $\ker \partial_n$ are called *cycles*, representing potential n -dimensional holes, while those in $\text{im } \partial_{n+1}$ are called *boundaries*, representing cycles that are filled in by higher-dimensional simplices. The true n -dimensional holes are captured by the *homology group*

$$H_n(K) = \ker \partial_n / \text{im } \partial_{n+1}.$$

Each homology group is a vector space, and its dimension records the number of independent n -dimensional holes. These invariants provide a compact algebraic summary of the underlying topological structure of the simplicial complex.

Persistent homology

We present a short overview of persistent homology. Suppose we have a population $P = \{p_1, \dots, p_n\}$ of interest that we wish to analyze. We assume that the pairwise dissimilarities between any pair p_i and p_j is known. A convenient way to encode the system is through a *simplicial complex* that has P as its vertex set. One way of obtaining this goal is to fix a threshold $\varepsilon > 0$ and construct the simplicial complex $X_P^\varepsilon = (P, F_\varepsilon)$, where the vertices are given by P and a subset $\sigma \subseteq P$ belongs to F_ε whenever all its members are at most ε apart. The first homology group $H_1(X_P^\varepsilon)$ then records the 1-dimensional cycles in this complex, with its dimension giving the number of independent loops present.

Choosing a single threshold ε can be arbitrary, however. Persistent homology addresses this by examining how the homology evolves as ε varies. Given a sequence of thresholds $\{\varepsilon_1 < \varepsilon_2 < \dots < \varepsilon_N\}$, one obtains a filtration of simplicial complexes

$$X_P^{\varepsilon_1} \subseteq X_P^{\varepsilon_2} \subseteq \dots \subseteq X_P^{\varepsilon_N}.$$

Applying homology to this nested sequence yields a diagram of vector spaces and linear maps,

$$(3) \quad H_1(X_P^\bullet) : H_1(X_P^{\varepsilon_1}) \rightarrow H_1(X_P^{\varepsilon_2}) \rightarrow \dots \rightarrow H_1(X_P^{\varepsilon_N}),$$

where each map arises from the inclusion of one simplicial complex into another, carrying cycles forward across scales. Persistent homology tracks when a homological feature (such as a cycle) first appears and when it disappears within this filtration.

The lifespan of a feature is summarized by its *birth* parameter b and *death* parameter d . Plotting the collection of points (b, d) gives the *persistence diagram*, a compact summary of the multi-scale topological structure. For a comprehensive treatment, see [6, 9, 10, 16]

A.2. Robustness against spontaneous firing. We report the reconstruction errors under varying levels of additional spontaneous firing of simulated grid cells. In the main text, we examine the robustness of the method under addition of one-dimensional Gaussian functions with peak height $h = 0.4$ (main text, Table 1). Here, we examine the reconstruction errors while varying the peak heights (0.08, 0.2, 0.3, and 0.4). See the following section for example firing rates after the addition of Gaussian noise.

%		Standard Deviation (σ)			
		1	10	50	100
Proportion (p)	0.1 %	1.831	1.616	1.677	1.658
	0.5 %	1.585	1.563	1.744	1.798
	1 %	1.575	1.639	1.776	1.992
	5 %	1.554	1.749	39.920	N/A
	10 %	1.665	1.995	N/A	N/A

Table 2. Reconstruction errors (%) computed with noise of peak height $h = 0.08$.

%		Standard Deviation (σ)			
		1	10	50	100
Proportion (p)	0.1 %	1.536	1.543	1.580	1.658
	0.5 %	1.546	1.696	1.923	21.232
	1 %	1.780	1.783	23.113	40.568
	5 %	1.691	11.645	N/A	N/A
	10 %	1.621	23.908	51.168	N/A

Table 3. Reconstruction errors (%) computed with noise of peak height $h = 0.2$.

%		Standard Deviation (σ)			
		1	10	50	100
Proportion (p)	0.1 %	1.594	1.614	1.639	2.030
	0.5 %	1.553	1.645	14.790	39.947
	1 %	1.590	1.773	22.926	122.375
	5 %	1.636	19.310	N/A	N/A
	10 %	11.977	100.915	N/A	N/A

Table 4. Reconstruction errors (%) computed with noise of peak height $h = 0.3$.

%		Standard Deviation (σ)			
		1	10	50	100
Proportion (p)	0.1 %	1.562	1.550	1.700	8.872
	0.5 %	1.559	1.731	16.976	77.131
	1 %	1.714	1.931	68.554	240.194
	5 %	5.824	23.778	N/A	N/A
	10 %	20.142	40.299	N/A	N/A

Table 5. Reconstruction errors (%) computed with noise of peak height $h = 0.4$.

A.3. Simulated grid cell activities with added Gaussian noise of different parameters h, p , and s . Here, we present a visualization of the simulated firing rates after adding Gaussian noise of varying parameters.

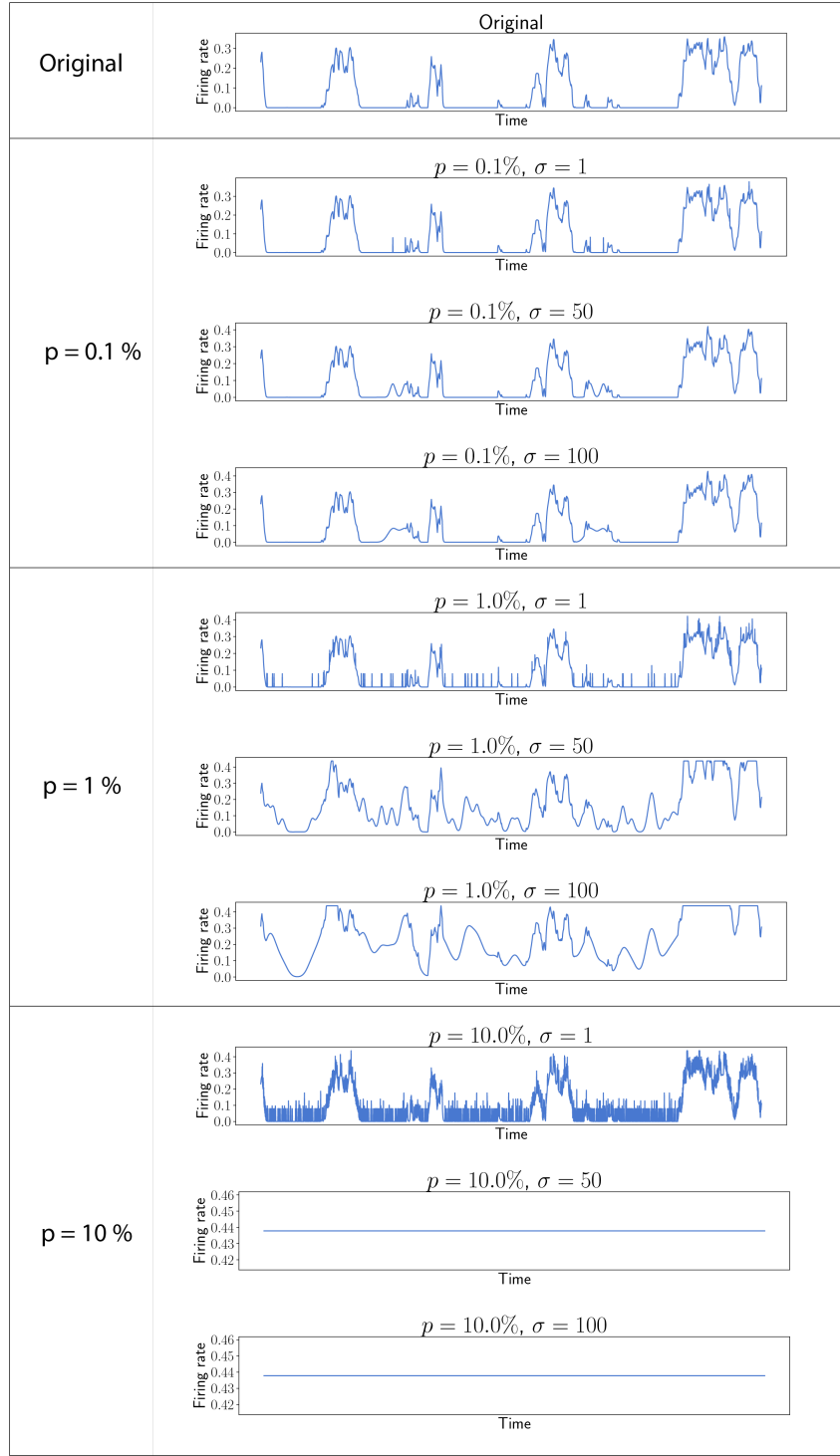


Figure SI-2. Simulated grid cell activities with added noise of different parameters of p and s . Peak heights h of the added noise is 0.08.

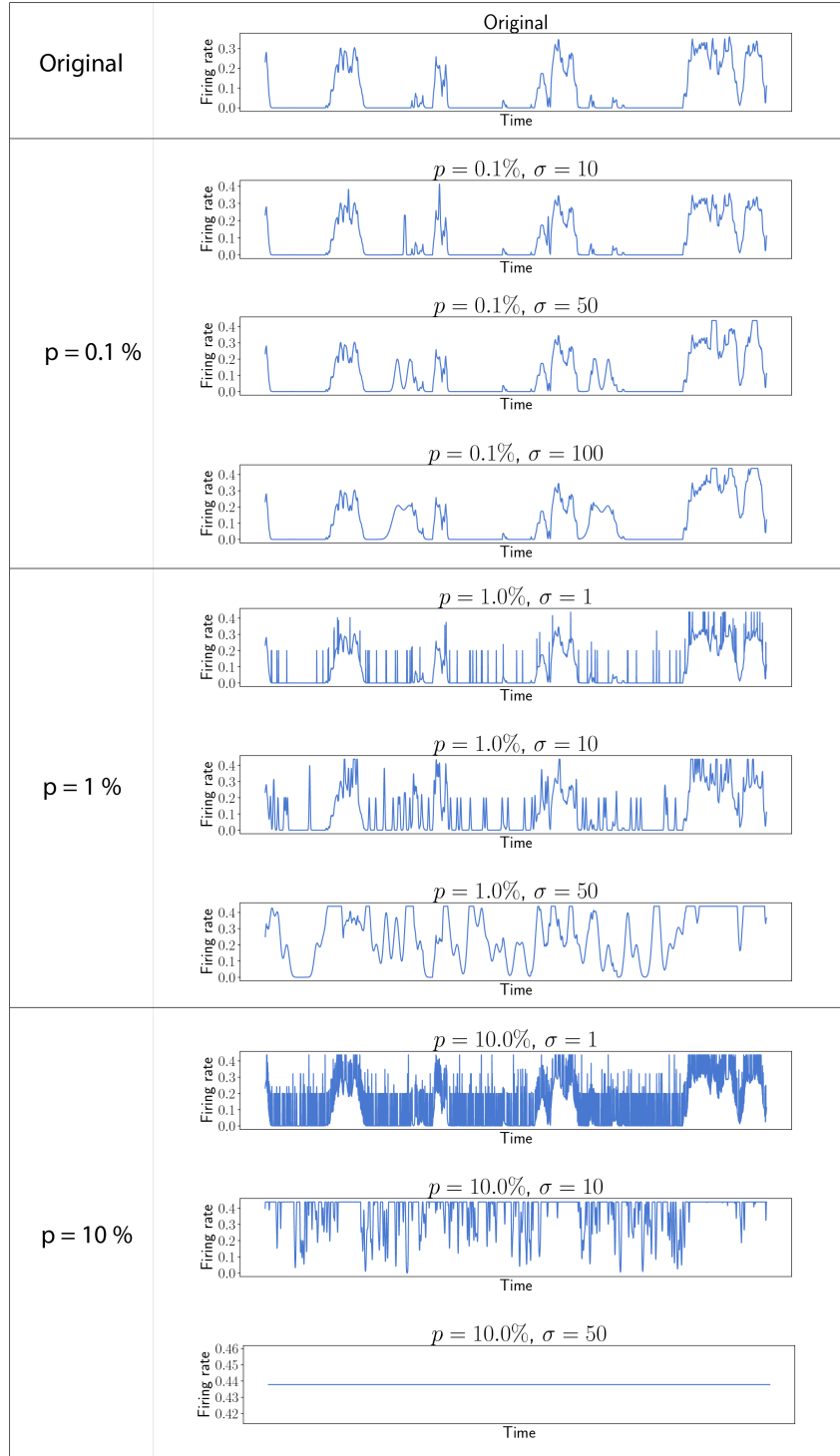


Figure SI-3. Simulated grid cell activities with added noise of different parameters of p and s . Peak height is fixed at $h = 0.2$.

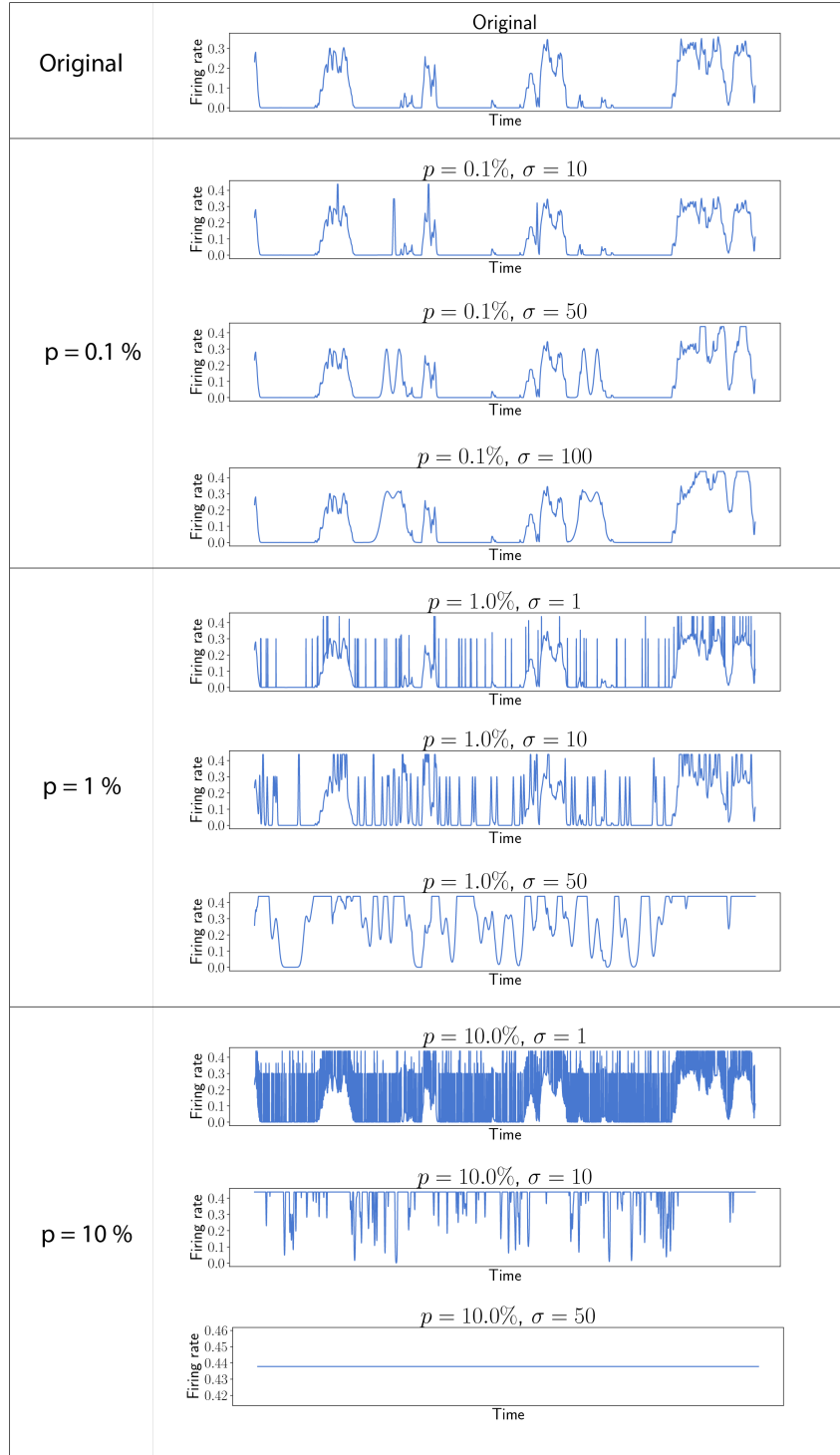


Figure SI-4. Simulated grid cell activities with added noise of different parameters of p and s . Peak height is fixed at $h = 0.3$.

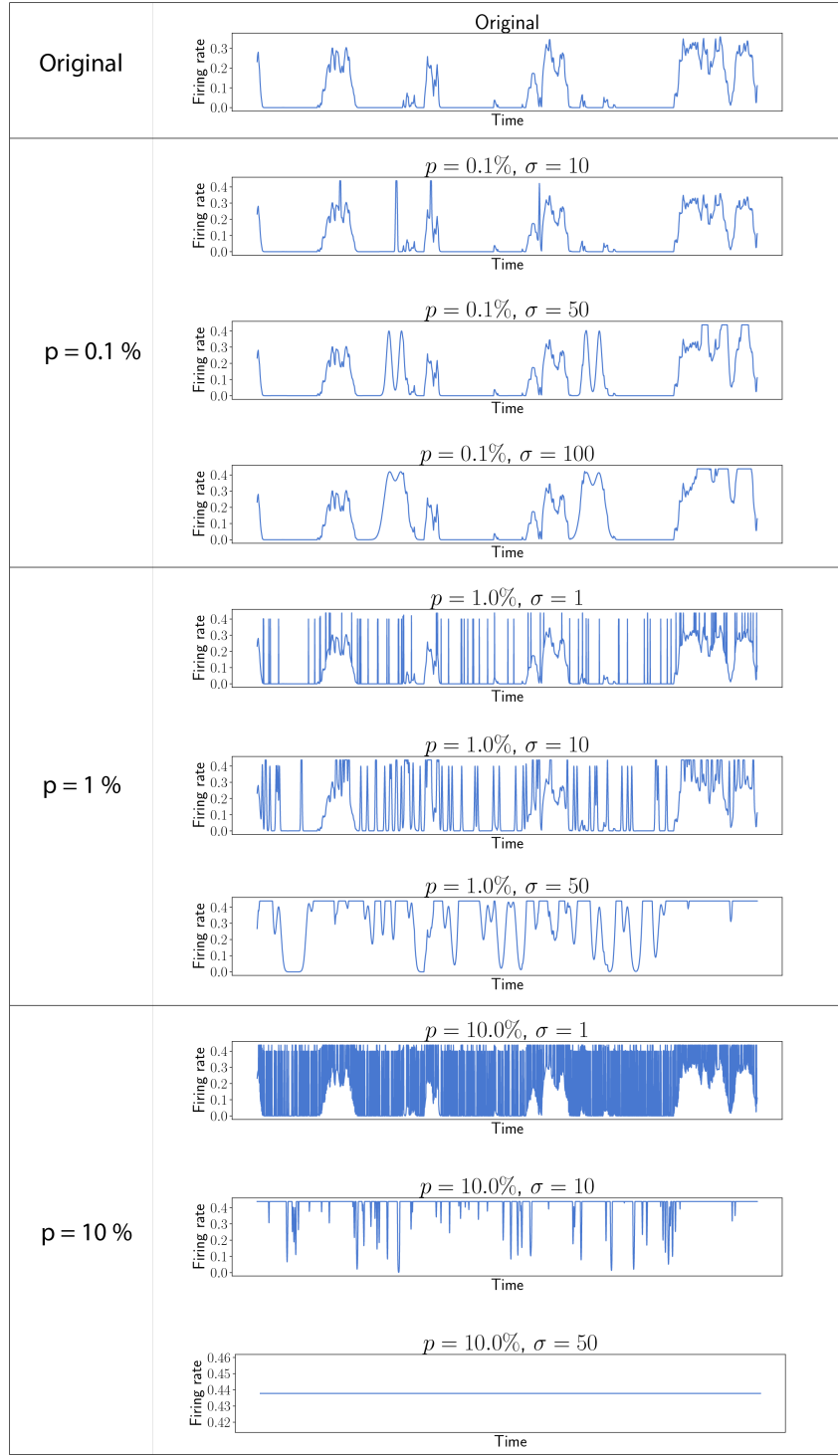


Figure SI-5. Simulated grid cell activities with added noise of different parameters of p and s . Peak height is fixed at $h = 0.4$.

A.4. Supplementary Figures.

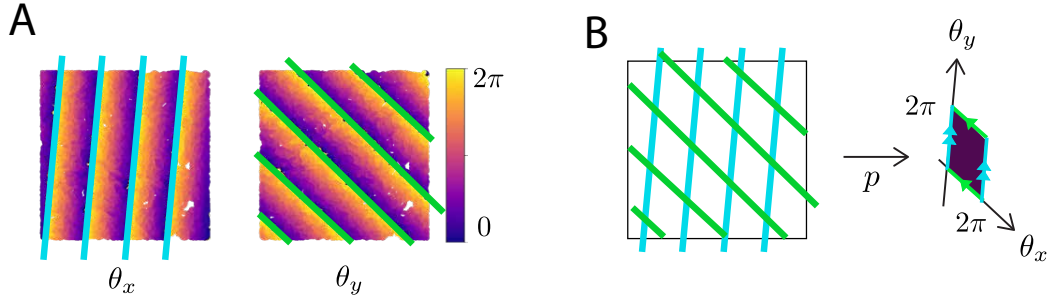


Figure SI-6. The toroidal coordinates define a tiling of \mathbb{R}^2 via parallelograms. **A.** An example visualization of the toroidal coordinates (θ_x, θ_y) . Here, given a time point t , let (x, y) denote the location of the mouse at time t . Let (θ_x^t, θ_y^t) be the toroidal coordinate assigned to population vector $P(t)$. The toroidal coordinates are visualized by a scatter plot in which a dot is placed at (x, y) whose color value represents θ_x^t (left) and θ_y^t (right). **B.** The toroidal coordinates define a tiling of \mathbb{R}^2 via parallelograms. The map p takes each parallelogram to one copy of the grid cell torus $S^1 \times S^1$.

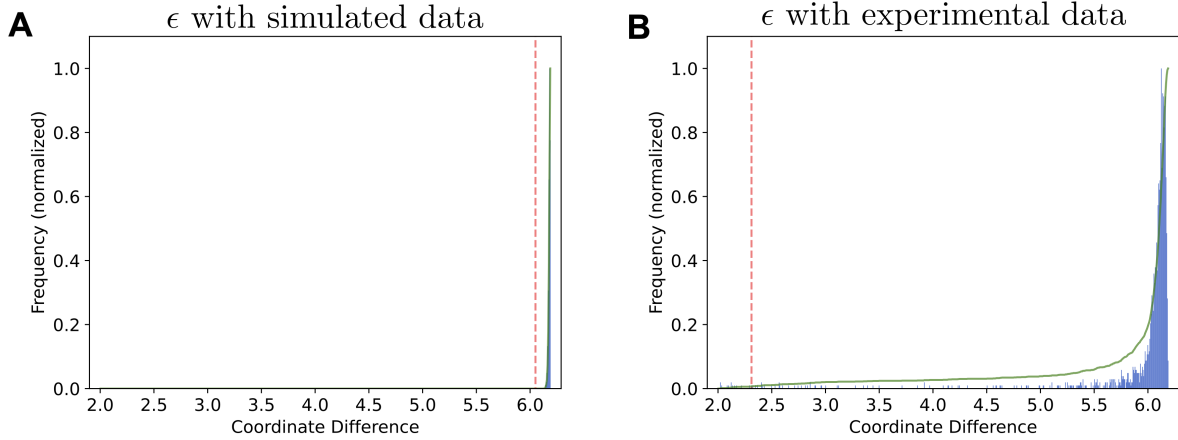


Figure SI-7. Proximity parameter ϵ from (A) simulated data and (B) two-dimensional experimental data [15]. The blue shows the histogram of the maximal coordinate differences, restricted to the range $[2, 2\pi]$, and the green curve shows their cumulative sum. The proximity parameter ϵ , shown in red dashed line, is selected as the parameter at which the CDF of the order-reversed coordinate differences first exceeds the threshold $\alpha = 0.99$ threshold.

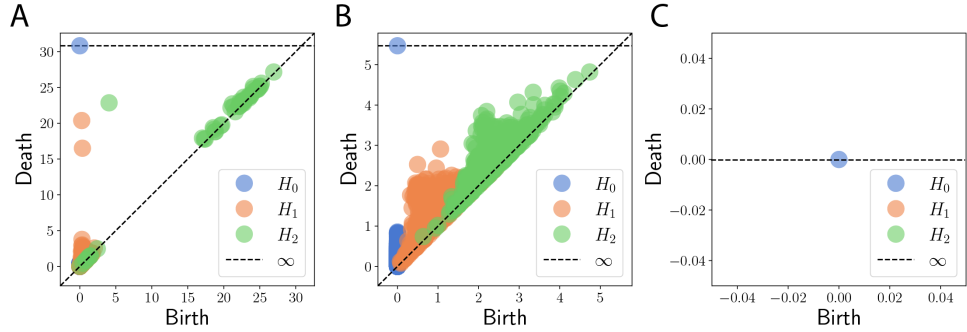


Figure SI-8. Example persistence diagrams that lead to low, high, and N/A reconstruction errors in the presence of spontaneous firings. **A.** Persistence diagram of the population vectors for $p = 0.05$ and $\sigma = 10$ has a clear toroidal structure, which leads to a low reconstruction error. **B.** Persistence diagram of the population vectors for $p = 0.05$ and $\sigma = 50$ does not have a clear toroidal structure, which leads to a high reconstruction error. **C.** Persistence diagram of the population vectors for $p = 0.05$ and $\sigma = 100$ has no non-trivial topological features. In such cases, the toroidal coordinates cannot be computed.

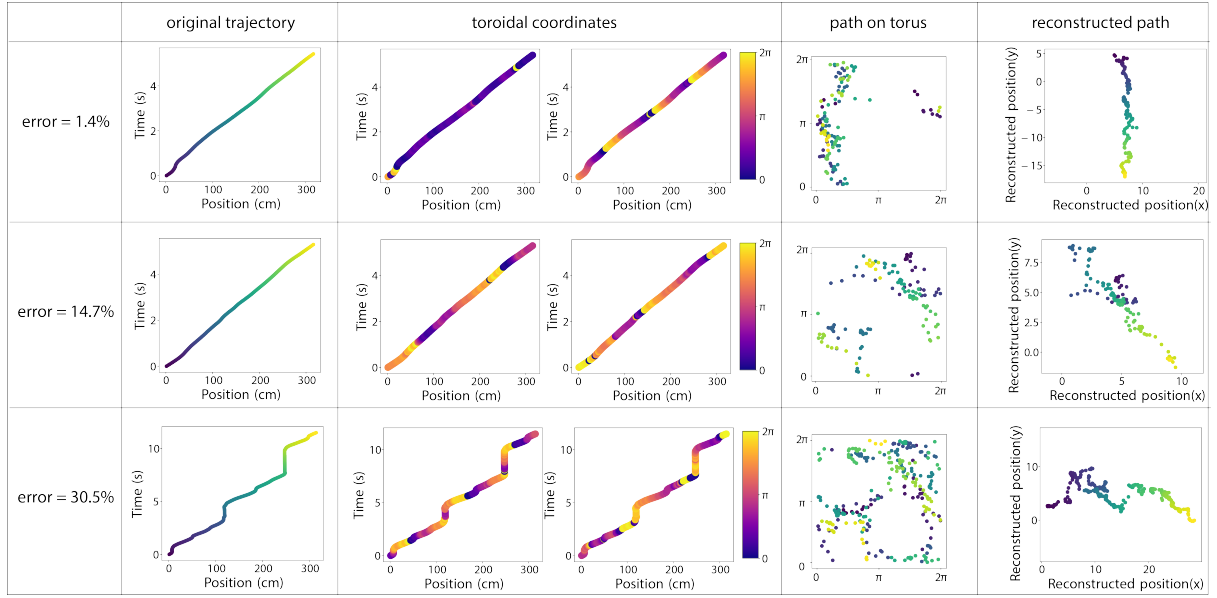


Figure SI-9. Example reconstructions with varying levels of reconstruction errors.

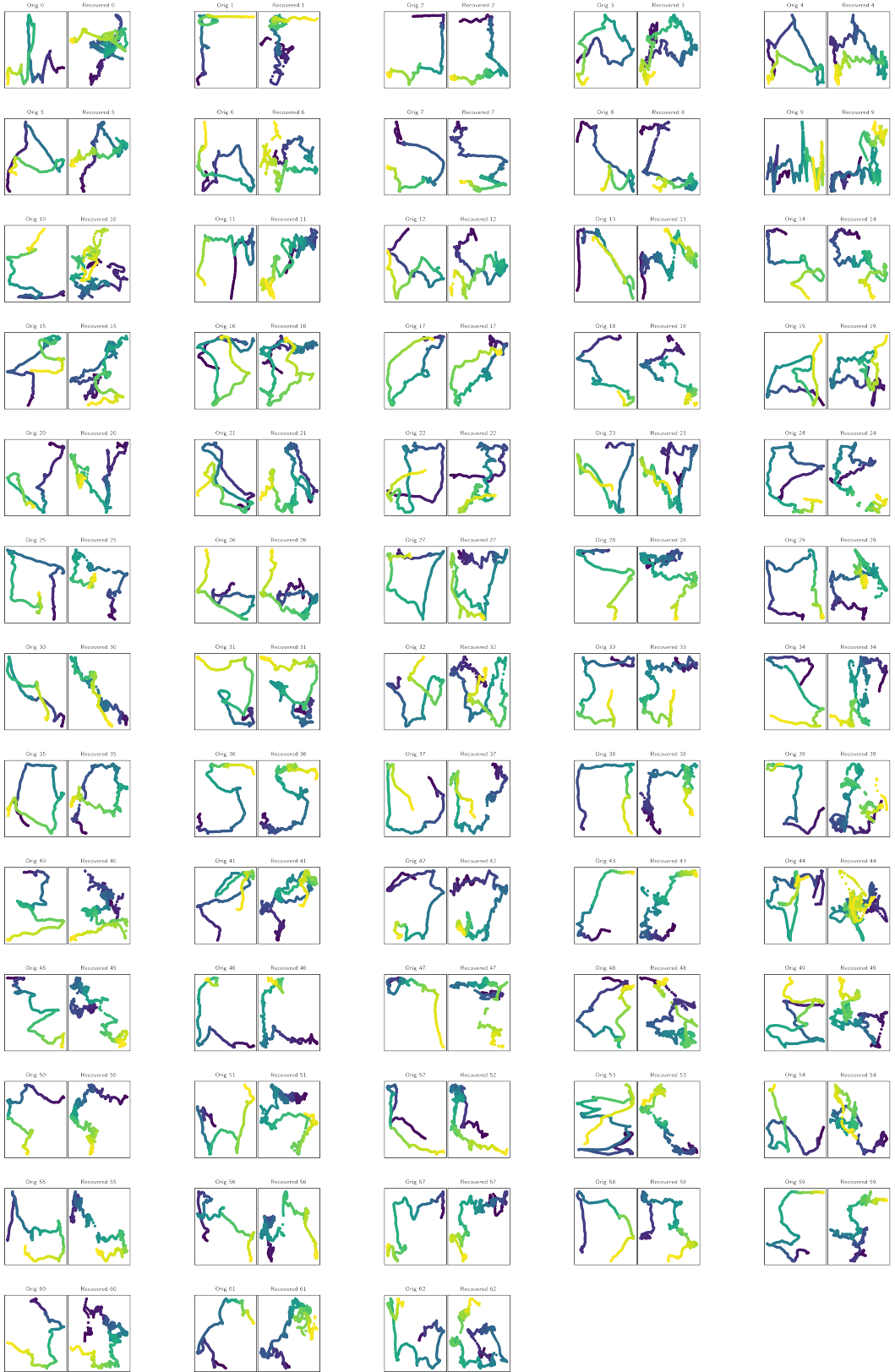


Figure SI-10. Complete local path reconstruction for two-dimensional experimental data from [15]. In each panel, the left sub-figure shows the original movement path, and right sub-figure visualizes the reconstructed movement path

REFERENCES

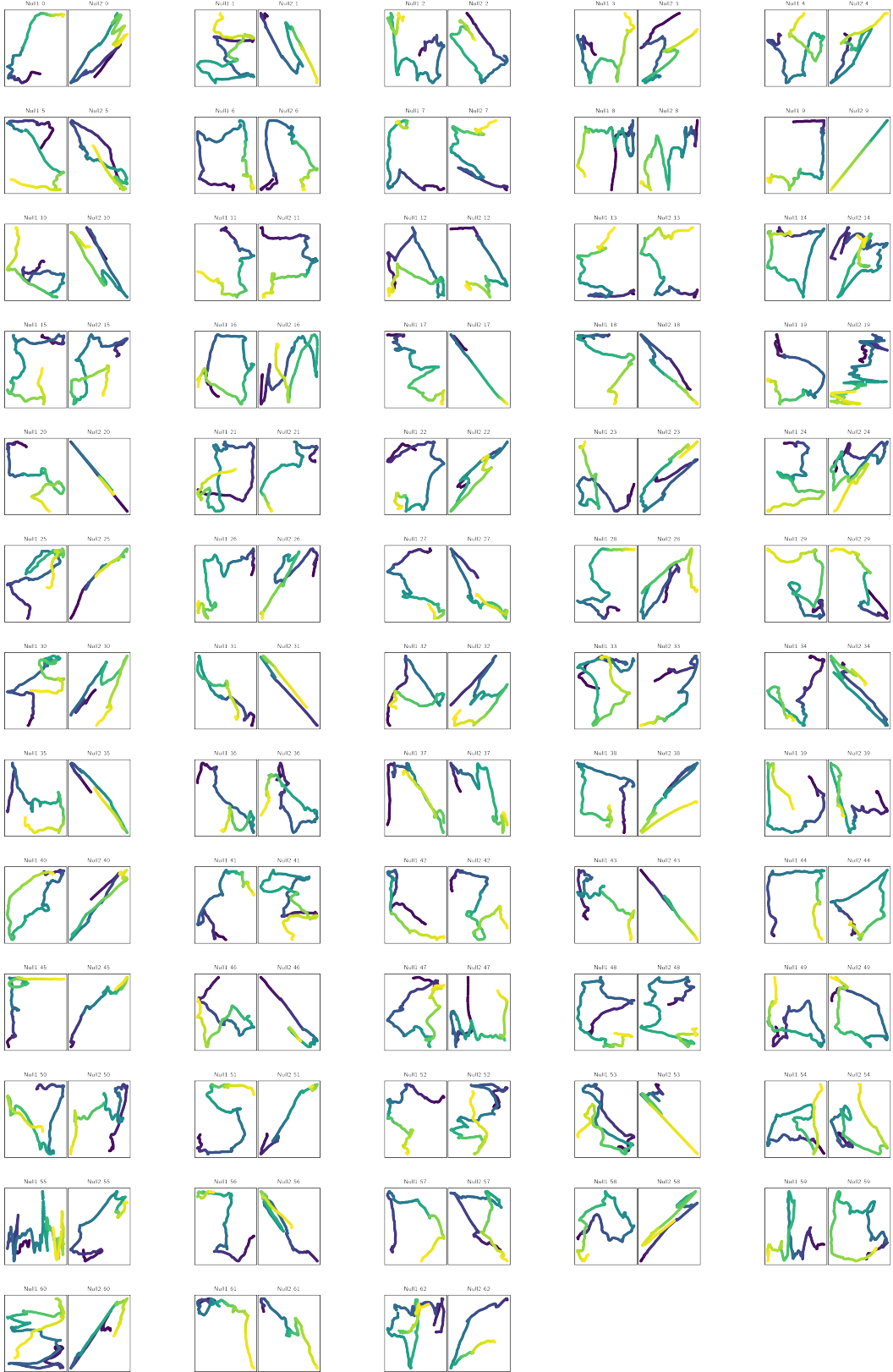


Figure SI-11. Example pairs of path segments of the original path in [15]. The errors between each pair is used to generate the distribution of reconstruction errors of the baseline case in main text Figure 7K. Each panel represents two path segments from the original path. In each panel, the left sub-figure shows a path segment, and the right sub-figure visualizes a randomly chosen path segment after the optimal affine transformation.

REFERENCES

- [1] C Barry and D Bush. *From A to Z: a potential role for grid cells in spatial navigation.* 523 *Neural Syst.* 2012.
- [2] Ulrich Bauer. “Ripser: efficient computation of Vietoris–Rips persistence barcodes”. In: *Journal of Applied and Computational Topology* 5.3 (2021), pp. 391–423.
- [3] G. Bradski. “The OpenCV Library”. In: *Dr. Dobb’s Journal of Software Tools* (2000).
- [4] Yoram Burak and Ila R Fiete. “Accurate path integration in continuous attractor network models of grid cells”. In: *PLoS computational biology* 5.2 (2009), e1000291.
- [5] Daniel Bush, Caswell Barry, Daniel Manson, and Neil Burgess. “Using grid cells for navigation”. In: *Neuron* 87.3 (2015), pp. 507–520.
- [6] Gunnar Carlsson. “Topology and Data”. In: *Bulletin of The American Mathematical Society - BULL AMER MATH SOC* 46 (Apr. 2009), pp. 255–308. DOI: [10.1090/S0273-0979-09-01249-X](https://doi.org/10.1090/S0273-0979-09-01249-X).
- [7] Rishidev Chaudhuri, Berk Gerçek, Biraj Pandey, Adrien Peyrache, and Ila Fiete. “The intrinsic attractor manifold and population dynamics of a canonical cognitive circuit across waking and sleep”. en. In: *Nature Neuroscience* 22.9 (Sept. 2019). Number: 9 Publisher: Nature Publishing Group, pp. 1512–1520. ISSN: 1546-1726. DOI: [10.1038/s41593-019-0460-x](https://doi.org/10.1038/s41593-019-0460-x).
- [8] Suogui Dang, Yining Wu, Rui Yan, and Huajin Tang. “Why grid cells function as a metric for space”. In: *Neural Networks* 142 (2021), pp. 128–137.
- [9] Herbert Edelsbrunner, John Harer, et al. “Persistent homology-a survey”. In: *Contemporary mathematics* 453.26 (2008), pp. 257–282.
- [10] Edelsbrunner, Letscher, and Zomorodian. “Topological persistence and simplification”. In: *Discrete & computational geometry* 28 (2002), pp. 511–533.
- [11] Uğur M Erdem and Michael Hasselmo. “A goal-directed spatial navigation model using forward trajectory planning based on grid cells”. In: *European Journal of Neuroscience* 35.6 (2012), pp. 916–931.
- [12] Ila R. Fiete, Yoram Burak, and Ted Brookings. “What Grid Cells Convey about Rat Location”. en. In: *Journal of Neuroscience* 28.27 (July 2008). Publisher: Society for Neuroscience Section: Articles, pp. 6858–6871. ISSN: 0270-6474, 1529-2401. DOI: [10.1523/JNEUROSCI.5684-07.2008](https://doi.org/10.1523/JNEUROSCI.5684-07.2008).
- [13] Markus Frey, Sander Tanni, Catherine Perrodin, Alice O’Leary, Matthias Nau, Jack Kelly, Andrea Banino, Christian F. Doeller, and Caswell Barry. *Deepinsight: a general framework for interpreting wide-band neural activity*. en. Pages: 871848 Section: New Results. Dec. 2019. DOI: [10.1101/871848](https://doi.org/10.1101/871848).
- [14] Mark C Fuhs and David S Touretzky. “A spin glass model of path integration in rat medial entorhinal cortex”. In: *Journal of Neuroscience* 26.16 (2006), pp. 4266–4276.
- [15] Richard J. Gardner, Erik Hermansen, Marius Pachitariu, Yoram Burak, Nils A. Baas, Benjamin A. Dunn, May-Britt Moser, and Edvard I. Moser. “Toroidal topology of population activity in grid cells”. In: *Nature* 602.7895 (Feb. 2022). Publisher: Nature Publishing Group, pp. 123–128. ISSN: 1476-4687. DOI: [10.1038/s41586-021-04268-7](https://doi.org/10.1038/s41586-021-04268-7).
- [16] Robert Ghrist. “Barcodes: the persistent topology of data”. In: *Bulletin of the American Mathematical Society* 45.1 (2008), pp. 61–75.
- [17] Torkel Hafting, Marianne Fyhn, Sturla Molden, May-Britt Moser, and Edvard I Moser. “Microstructure of a spatial map in the entorhinal cortex”. In: *Nature* 436.7052 (2005), pp. 801–806.
- [18] D. H. Hubel and T. N. Wiesel. “Receptive fields and functional architecture of monkey striate cortex”. eng. In: *The Journal of Physiology* 195.1 (Mar. 1968), pp. 215–243. ISSN: 0022-3751. DOI: [10.1113/jphysiol.1968.sp008455](https://doi.org/10.1113/jphysiol.1968.sp008455).
- [19] Jesse A Livezey and Joshua I Glaser. “Deep learning approaches for neural decoding across architectures and recording modalities”. In: *Briefings in Bioinformatics* 22.2 (Dec. 2020). eprint: <https://academic.oup.com/bib/article-pdf/22/2/1577/36654842/bbaa355.pdf>, pp. 1577–1591. ISSN: 1477-4054. DOI: [10.1093/bib/bbaa355](https://doi.org/10.1093/bib/bbaa355).

[20] Cécile Masson and Benoît Girard. “Decoding the Grid Cells for Metric Navigation Using the Residue Numeral System”. In: *Advances in Cognitive Neurodynamics (II)*. Ed. by Rubin Wang and Fanji Gu. Dordrecht: Springer Netherlands, 2011, pp. 459–464. ISBN: 978-90-481-9695-1.

[21] Alexander Mathis, Andreas VM Herz, and Martin Stemmler. “Optimal population codes for space: grid cells outperform place cells”. In: *Neural computation* 24.9 (2012), pp. 2280–2317.

[22] Bruce L McNaughton, Francesco P Battaglia, Ole Jensen, Edvard I Moser, and May-Britt Moser. “Path integration and the neural basis of the ‘cognitive map’”. In: *Nature Reviews Neuroscience* 7.8 (2006), pp. 663–678.

[23] Edward C. Mitchell, Brittany Story, David Boothe, Piotr J. Franaszczuk, and Vasileios Maroulas. “A topological deep learning framework for neural spike decoding”. English. In: *Biophysical Journal* 123.17 (Sept. 2024). Publisher: Elsevier, pp. 2781–2789. ISSN: 0006-3495, 1542-0086. DOI: [10.1016/j.bpj.2024.01.025](https://doi.org/10.1016/j.bpj.2024.01.025).

[24] J. Munkres. *Topology*. Pearson Modern Classics for Advanced Mathematics Series. Pearson, 2017. ISBN: 9780134689517.

[25] John O’Keefe. “Place units in the hippocampus of the freely moving rat”. In: *Experimental Neurology* 51.1 (Jan. 1976), pp. 78–109. ISSN: 0014-4886. DOI: [10.1016/0014-4886\(76\)90055-8](https://doi.org/10.1016/0014-4886(76)90055-8).

[26] Jing-Jie Peng, Beate Throm, Maryam Najafian Jazi, Ting-Yun Yen, Hannah Monyer, and Kevin Allen. *Grid cells perform path integration in multiple reference frames during self-motion-based navigation*. en. Pages: 2023.12.21.572857 Section: New Results. Dec. 2023. DOI: [10.1101/2023.12.21.572857](https://doi.org/10.1101/2023.12.21.572857).

[27] Jose A. Perea, Luis Scoccola, and Christopher J. Tralie. “DREiMac: Dimensionality Reduction with Eilenberg-MacLane Coordinates”. In: *Journal of Open Source Software* 8.91 (2023), p. 5791. DOI: [10.21105/joss.05791](https://doi.org/10.21105/joss.05791).

[28] Erik Rybakken, Nils Baas, and Benjamin Dunn. “Decoding of Neural Data Using Cohomological Feature Extraction”. In: *Neural Computation* 31.1 (Jan. 2019), pp. 68–93. ISSN: 0899-7667. DOI: [10.1162/neco_a_01150](https://doi.org/10.1162/neco_a_01150).

[29] Luis Scoccola, Hitesh Gakhar, Johnathan Bush, Nikolas Schonsheck, Tatum Rask, Ling Zhou, and Jose A. Perea. “Toroidal Coordinates: Decorrelating Circular Coordinates with Lattice Reduction”. In: *LIPICS, Volume 258, SoCG 2023* 258 (2023). In collab. with Erin W. Chambers and Joachim Gudmundsson. Artwork Size: 20 pages, 6894838 bytes ISBN: 9783959772730 Medium: application/pdf Publisher: Schloss Dagstuhl – Leibniz-Zentrum für Informatik, 57:1–57:20. ISSN: 1868-8969. DOI: [10.4230/LIPICS.SOCG.2023.57](https://doi.org/10.4230/LIPICS.SOCG.2023.57).

[30] Vin de Silva, Dmitriy Morozov, and Mikael Vejdemo-Johansson. “Persistent Cohomology and Circular Coordinates”. en. In: *Discrete & Computational Geometry* 45.4 (June 2011), pp. 737–759. ISSN: 1432-0444. DOI: [10.1007/s00454-011-9344-x](https://doi.org/10.1007/s00454-011-9344-x).

[31] Trygve Solstad, Edvard I Moser, and Gaute T Einevoll. “From grid cells to place cells: a mathematical model”. In: *Hippocampus* 16.12 (2006), pp. 1026–1031.

[32] Martin Stemmler, Alexander Mathis, and Andreas VM Herz. “Connecting multiple spatial scales to decode the population activity of grid cells”. In: *Science Advances* 1.11 (2015), e1500816.

[33] Hong Sun and Tian-Ren Yao. “A neural-like network approach to residue-to-decimal conversion”. In: *Proceedings of 1994 IEEE International Conference on Neural Networks (ICNN’94)*. Vol. 6. June 1994, 3883–3887 vol.6. DOI: [10.1109/ICNN.1994.374831](https://doi.org/10.1109/ICNN.1994.374831).

[34] Ardi Tampuu, Tambet Matiisen, H. Freyja Ólafsdóttir, Caswell Barry, and Raul Vicente. “Efficient neural decoding of self-location with a deep recurrent network”. en. In: *PLOS Computational Biology* 15.2 (Feb. 2019). Publisher: Public Library of Science, e1006822. ISSN: 1553-7358. DOI: [10.1371/journal.pcbi.1006822](https://doi.org/10.1371/journal.pcbi.1006822).

[35] Jeffrey S Taube, Robert U Muller, and James B Ranck. “Head-direction cells recorded from the postsubiculum in freely moving rats. I. Description and quantitative analysis”. In: *Journal of Neuroscience* 10.2 (1990), pp. 420–435.

- [36] Christopher Tralie, Nathaniel Saul, and Rann Bar-On. “Ripser. py: A lean persistent homology library for python”. In: *Journal of Open Source Software* 3.29 (2018), p. 925.
- [37] Vincent Villette, Arnaud Malvache, Thomas Tressard, Nathalie Dupuy, and Rosa Cossart. “Internally Recurring Hippocampal Sequences as a Population Template of Spatiotemporal Information”. eng. In: *Neuron* 88.2 (Oct. 2015), pp. 357–366. ISSN: 1097-4199. DOI: [10.1016/j.neuron.2015.09.052](https://doi.org/10.1016/j.neuron.2015.09.052).
- [38] John H Wen, Ben Sorscher, Emily A Aery Jones, Surya Ganguli, and Lisa M Giocomo. “One-shot entorhinal maps enable flexible navigation in novel environments”. In: *Nature* 635.8040 (2024), pp. 943–950.
- [39] Zishen Xu, Wei Wu, Shawn S. Winter, Max L. Mehlman, William N. Butler, Christine M. Simmons, Ryan E. Harvey, Laura E. Berkowitz, Yang Chen, Jeffrey S. Taube, Aaron A. Wilber, and Benjamin J. Clark. “A Comparison of Neural Decoding Methods and Population Coding Across Thalamo-Cortical Head Direction Cells”. English. In: *Frontiers in Neural Circuits* 13 (Dec. 2019). Publisher: Frontiers. ISSN: 1662-5110. DOI: [10.3389/fncir.2019.00075](https://doi.org/10.3389/fncir.2019.00075).
- [40] Yuansheng Zhou, Brian H. Smith, and Tatyana O. Sharpee. “Hyperbolic geometry of the olfactory space”. In: *Science Advances* 4.8 (Aug. 2018). Publisher: American Association for the Advancement of Science, eaaq1458. DOI: [10.1126/sciadv.aaq1458](https://doi.org/10.1126/sciadv.aaq1458).